An Estimate of the Upwelling Rate in the Tropical Pacific Ocean

by

Sarah Louise Samuel

B.A., Somerville College, Oxford University
(1996)

MRes., The University of Edinburgh
(1997)

Submitted to the Department of Earth, Atmospheric and Planetary Sciences
in partial fulfillment of the requirements for the degree of

Master of Science in Climate Physics and Chemistry

at the

MASSACHUSETTS INSTITUTE OF TECHNOLOGY

October 1999
[February 2000]

Author .....
Department of Earth, Atmospheric and Planetary Sciences
October 21, 1999

Certified by .....
Carl I. Wunsch
Professor
Thesis Supervisor

Accepted by .....
Ronald G. Prinn
Head, Department of Earth, Atmospheric and Planetary Sciences

An Estimate of the Upwelling Rate in the Tropical Pacific Ocean

by

Sarah Louise Samuel

B.A., Somerville College, Oxford University

(1996)

MRes., The University of Edinburgh

(1997)

Submitted to the Department of Earth, Atmospheric and Planetary Sciences
on October 21, 1999, in partial fulfillment of the
requirements for the degree of
Master of Science in Climate Physics and Chemistry

Abstract

An inverse box model of the tropical Pacific Ocean from 32°S – 10°N is constructed from two zonal and six meridional hydrographic sections. This data is supplemented with LADCP data close to the equator where geostrophy fails. A consistent solution is found despite the presence of a number of mid-ocean crossing points and the data being spread over many years and seasons. The total upwelling across the $\sigma_\theta = 23.5$ isopycnal surface in a 6^0 latitude band centered on the equator is estimated to be $55 \pm 27Sv$. The zonal mean cross-isopycnal velocity for the same surface in the same latitude band is estimated to be $6.88 \pm 3.23 \times 10^{-4} cms^{-1}$.

The addition of radiocarbon data places a strong constraint on the vertical transfers in the model and significantly reduces the error on the estimated vertical transport and velocity. When radiocarbon constraints are included, the upwelling across the $\sigma_\theta = 23.5$ isopycnal surface in the equatorial zone is estimated to be $52 \pm 16Sv$ and the zonal mean cross-isopycnal velocity across the same surface is estimated as

$7.15 \pm 1.90 \times 10^{-4} cms^{-1}$.

That a consistent solution can be found is encouraging but it remains unclear whether one-time data is representative of mean conditions in a region which is known to be highly variable.

Thesis Supervisor: Carl I. Wunsch
Title: Professor

Acknowledgments

Although the cover page of this thesis bears only one name, I would not have been able to complete this task without the support and guidance, scientific or otherwise, of many people over many years.

First, I must thank those who gave me help specifically associated with this work. Carl Wunsch, my thesis advisor, has provided support throughout my time as a graduate student at MIT and has shown great patience whilst I grappled with problems. Robert Key kindly provided the radiocarbon data and a wealth of advice on how to deal with it; Eric Firing supplied the LADCP data and Susan Wijffels provided the mean hydrographic data. I am enormously indebted to Alexandre Ganachaud who wrote the wondrous Hydrosys Matlab routines and saved me from many months of programming and to Alison MacDonald who gave me thoughtful advice and positive guidance. This work was supported by Caltech J.P.L. contract 958125; NSF/WOCE contract OCE-9730071 and NASA/WOCE contract NAG5-7857.

Many others have been essential to the completion of this project in many ways: Scott Sewell gave a sympathetic ear and advice (not to mention chocolate) when I was at my most despairing and uttered the phrase that has been my guiding light for the last 9 months: "...you'll have your masters, you'll be in Fiji and you'll be a happy woman". Patricia Kassis (née Bradshaw) did most of my problem sets for me and taught me everything I know about "Them Broncos!". One (or all) of Veronique Bugnion, Will Heres and Jessica Neu were always willing to be distracted from their work on the 17th floor and Mary Elliff frequently helped out with particularly tricky problems, such as sending a fax. Gerard Roe was always willing to give sage advice, especially over a pint and Christopher Barrett rarely refused an invitation to The Misery. Thanks are also due to Rebecca Morss, Mort Webster, Nili Harnik, Constantine Giannitsis, Geri Campos and Jenn Jamieson.

The staff and volunteers of Youth Enrichment Services enormously enriched *my* life and provided a retreat from the rigours of academic study. The "Wednesday night fitters" including Steve Murray, Trish Gallagher, Dee Cassidy, Jeff Mills, Verena Jones, Coleen Sebastien, Sarah Olson *et al.* made hectic evenings in the shop great fun, and Richard Williams, Mary Crowther and Eric Pickney were always kind and appreciative. The kids were always challenging and even more rewarding—especially Carlos and Trisha, my two top pupils, who inspired me with their enthusiasm and joy.

Many friends in the UK and other exotic locales (notably Fiji) have supplied encouragement, Ribena and Marmite as need. My sister, Claire Samuel, frequently sent chocolate and was always ready to commiserate and my parents, Ronald and Ann Samuel, continue to tolerate their daughters' apparent disinclination to become gainfully employed. And to fulfill a two-year old promise, thanks to Caroline Ross for the tea, Vix Snell for the right sleeve and Claire Marshall for the left sleeve.

Finally, my thanks to three people who I have shared so much with: Antonio Irranca has been a constant companion over the last three years - thanks for being the froth on the cappucino of my life; Molly Frey was a wonderful roommate and continues to supply many happy evenings of conversation and friendship and Albert Fischer, what can I say? Friend, technical support, travel consultant and so much more - Thank you.

Contents

List of Figures

List of Tables

Chapter 1

Introduction

Understanding the role of the oceans in the global carbon cycle is key to understanding the climate system as a whole. The equatorial Pacific Ocean is particularly significant since this region is the major ocean source of carbon dioxide to the atmosphere [*Tans et al.*, 1990]. CO_2 is released from the ocean when deep waters upwell and are warmed at the ocean surface and so a good estimate of vertical transport is necessary as this is the major control on the surface exchange.

1.1 Previous work

Vertical velocities are small and difficult to measure directly so estimates of upwelling are either inferred from other observations or calculated in general circulation models. The highest upwelling rates are confined to a narrow band centered on the equator and away from the equator there is downwelling and so estimates are strongly effected by the area over which they are made.

Quay et al. [1983] made an estimate using measurements of ^{14}C made during the NORPAX Shuttle experiment in a two-dimensional (north-south and depth) multi-

layer mixing model. They estimated a upwelling transport rate of $47 \pm 13 Sv$ associated with a vertical velocity of $110 \pm 30 myr^{-1}$ (approximately $3.5 \pm 1 \times 10^{-4} cms^{-1}$) across the base of the mixed layer in the region 5°S – 4°N and 170°E – 100°W. *Bryden and Brady* [1985] estimated a vertical transport of 22 Sv and velocity of $2.9 \times 10^{-3} cms^{-1}$ from a three-dimensional diagnostic model applied to data in the region 5°N - 5°S and 150°W - 110°W and *Wijffels* [1993] estimated 60 Sv and velocities of order $2 \times 10^{-4} cms^{-1}$ in an area from 15°S - 8°N and 165°E to the eastern boundary from an inverse model.

Studies which have focused on the region closer to the equator typically give higher estimates of the maximum vertical transfer. *Philander et al.* [1987] diagnosed vertical velocities of over 400 cmday^{-1} (around $5 \times 10^{-3} cms^{-1}$) and vertical transport in a 5^o latitude band centered on the equator of some 114 Sv. *Poulain* [1993] focused on a 20km latitude band either side of the equator and derived an estimate of $1.5 - 2 \times 10^{-3} cms^{-1}$ by requiring the vertical velocity to balance the horizontal divergence computed from the trajectories of satellite-tracked surface drifters and a more recent study by *Harrison* [1996] estimated 200cmday^{-1} between $2^oS - 2^oN$ at 140° W using a state-of-the-art ocean circulation model.

1.2 Outline of thesis

In this work, a new estimate of vertical transport is made based on the recent measurements of radiocarbon from the WOCE Pacific Ocean radiocarbon program [*Key*, 1996; *Key et al.*, 1996; *Stuiver et al.*, 1996]. The atmospheric testing of nuclear weapons in the 1960s introduced a large perturbation to the natural ^{14}C cycle. Bomb-^{14}C is absorbed by the oceans at the surface and its vertical distribution in the ocean may be considered as a balance between the rate of invasion and the rate of upwelling and advection of bomb-^{14}C free waters.

In Chapter 2, the setup of the basic mass, heat and salt conserving model is described and some results presented. The full model including the radiocarbon constraints is discussed in chapter 3. Limitations of the current model and possible improvements and future work are discussed in chapter 4.

Chapter 2

Steady State Model

An inverse box model is used to obtain an estimate of the circulation in the tropical Pacific Ocean. Hydrographic and lowered acoustic Doppler current profilemeter (LADCP) data is used as to make the initial estimate of the flow field and the system solved using Gauss-Markov estimation. An estimate of the zonal mean equatorial upwelling and cross-isopycnal velocity is made.

2.1 Initial Flow Estimates

2.1.1 Hydrographic data

The hydrographic data used in this model consisted of two basin-wide zonal sections and six meridional sections. All of these were collected as part of the World Ocean Circulation Experiment (WOCE) and in this thesis I shall refer to them using their WOCE labels. The positions of the sections along with the dates of the cruises and the section labels are shown in Figure 2-1. The stations at the western end of P4 were replaced with mean stations since the Mindanao current was anomalously strong when the measurements for P4 were made [*Wijffels*, 1993; *Wijffels et al.*, 1995].

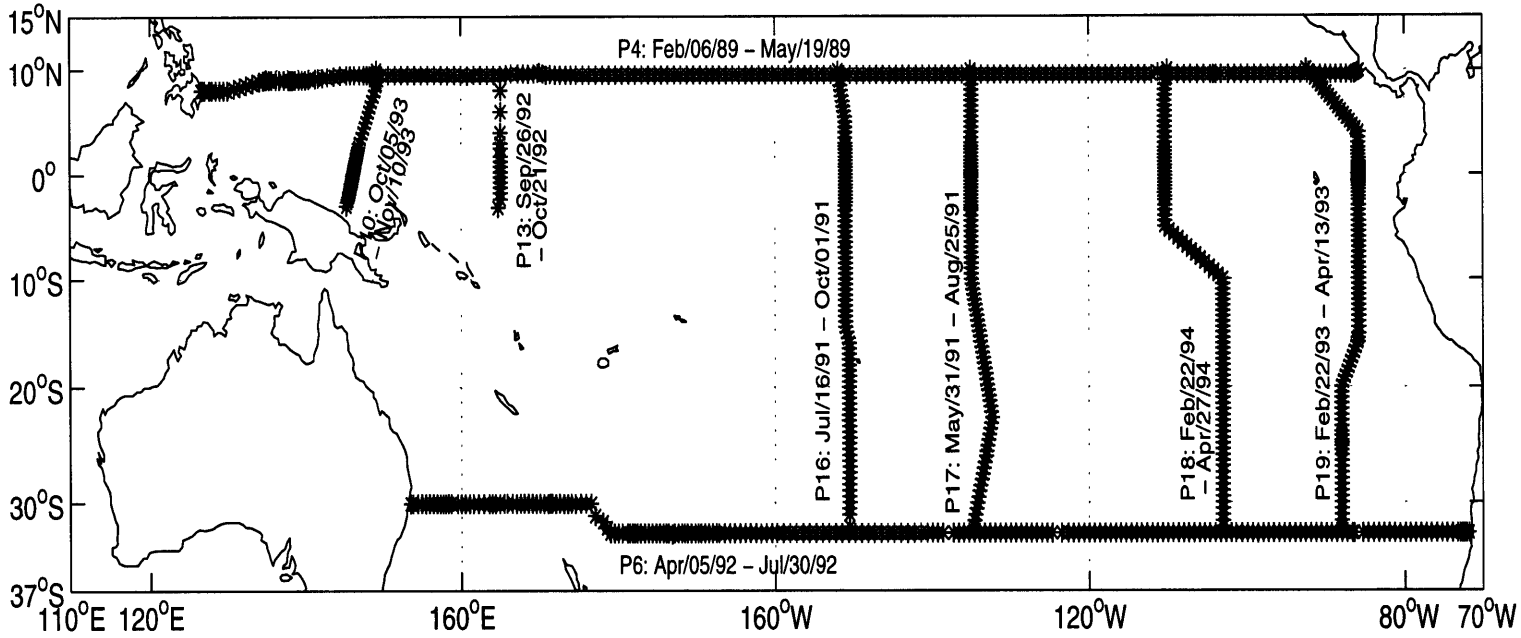

Figure 2-1: Map showing the positions of the hydrographic data sections used along with the WOCE labels for each section and the dates of the cruises

The temperature and salinity data were interpolated onto a standard grid of 50 *db* intervals from 0 *db* to 8000 *db*. Geostrophic velocities, perpendicular to each section, were calculated using the thermal wind equations:

$$u_g = -\frac{g}{f\rho}\int_{z_o}^{z}\frac{\partial\rho}{\partial y}\,dz \tag{2.1a}$$

$$v_g = \frac{g}{f\rho}\int_{z_o}^{z}\frac{\partial\rho}{\partial x}\,dz \tag{2.1b}$$

where: g acceleration due to gravity

$f(=2\Omega\sin\theta)$ Coriolis parameter,

(Ω is the Earth's rate of rotation and θ is latitude)

ρ density

x, y zonal and meridional directions

z depth

u_g, v_g zonal and meridional geostrophic velocities at depth z relative to those at depth z_o

The reference level, z_o, was taken as 3000 *db* *, the approximate depth of the boundary between the slow moving deep and bottom waters of the Pacific. Temperature and salinity for a station pair is taken to be the mean of the two stations.

2.1.2 LADCP data

Close to the equator, geostrophy cannot be applied in this form since f becomes very small. However, in the long term mean, geostrophy *is* an adequate approximation for the *zonal* component of the flow [*Pedlosky*, 1996]. The equatorial geostrophic

*The small difference between depth in m and pressure in *db* is neglected

balance, equation 2.2, is obtained by differentiating equation 2.1a with respect to y [*Arthur*, 1960].

$$u_g = -\frac{1}{\rho\beta}\frac{\partial^2 p}{\partial y^2} \tag{2.2}$$

where $\beta = \frac{\partial f}{\partial y}$, is the meridional gradient of the Coriolis parameter and p is pressure.

No reasonable estimate of the equatorial flow field could be found even when the data were smoothed using either a quadratic fit [*Johnson and Toole*, 1993] or a quartic fit [*Wijffels*, 1993]. This is unsurprising since, in previous work, this balance has been applied to composite hydrographic sections where mean observations have been derived from many different surveys in different years and seasons. The data used here are a one-time survey and the equatorial geostrophic balance is particularly sensitive to variability and error in the observations: a change in dynamic height of only $0.01 Jkg^{-1}$ † at the equator results in a change in geostrophic velocity of $7.1 cms^{-1}$ [*Bryden and Brady*, 1985].

As a result of these difficulties, the flow field within 3^o of the equator was estimated using the LADCP data collected on each cruise [*Firing et al.*, 1998]. These are measurements of absolute velocity and this was accounted for in the model by setting the variance of the reference level velocity to zero in the columns where this data was used.

Defined 'sections'

Two zonal 'sections' were defined at $\pm 3^o$ using the stations from each meridional section that was closest to the given latitude and the geostrophic velocities calculated using equation 2.1b. It was assumed that the the station pair properties for the most easterly pair represented the ocean state right up to the eastern boundary. These

† $1 Jkg^{-1}$ = 1 'dynamic decimeter' = 10 dyn cm

sections are likely to be the least satisfactory in the model since each consists of only six data points spread over several years in time. The section at 3°N will be referred to as P41 and that at 3°S as P42.

2.1.3 Ekman fluxes

The Ekman transport across each section, or section segment, was estimated using the Southampton Oceanography Centre (SOC) monthly wind stress climatology [*Josey et al.*, 1996]. The fields were derived from the Comprehensive Atmosphere–Ocean Dataset (COADS) Release 1a and supplemented with information about observing practices on different ships from the World Meteorological Organisation (WMO) [*ibid.*]. The data consisted of the monthly mean northward and eastward components of wind stress on a 1° latitude by 1° longitude grid from 31.5°S to 9.5°N and from 120°E to 70°W. From this, the annual mean wind stress was computed and the Ekman flux calculated using the equations

$$T_{Ek_x} = \sum_{i=1}^{N} \frac{\tau_i^y \Delta y_i}{f_i} \qquad T_{Ek_y} = \sum_{i=1}^{N} \frac{-\tau_i^x \Delta x_i}{f} \tag{2.3}$$

where T_{Ek} Ekman transport normal to the stress direction

N number of stations in section segment

τ wind stress

$\Delta x_i, \Delta y_i$ width of gridbox i

The annual mean wind stress is the most appropriate to use since I am assuming the hydrography represents a mean state [*Jayne*, 1999].

2.1.4 Indonesian Throughflow

The published range of estimates for the flow through the Indonesian Passages is large—*Fieux et al.* [1996] gave a range of 1-22 Sv. In this model, I use the most recent available estimate of $14 \pm 4Sv$ [*Ganachaud*, 1999].

2.1.5 Validity of assumptions

All of the above discussion assumes that the initial data are representative of the long term mean and that the circulation is in geostrophic balance. Both of these assumptions are suspect. The tropical Pacific Ocean is known to be a region of very high variability and the dataset may not even be self consistent, since the observations were taken in different seasons and in different years. *Takahashi et al.* [1997] list as El-Niño periods: Oct 91 - May 92; Oct 92 - Oct 93 and Apr 94 - Feb 95 so sections P10 and P19 were both taken during El-Niños. During such episodes, upwelling in the eastern Pacific is much weaker than usual and temperatures in the upper water column are increased. The equatorial regions are also the area where geostrophy is most difficult to apply. The geostrophic balance is not valid at the equator and is very noisy close to the equator due to the small size of f and the signal of ageostrophic motions in the temperature and salinity fields. Nevertheless, in order to proceed, these assumptions will be kept.

2.2 Model Formulation

2.2.1 Model Areas

The region covered by the model was divided into 24 overlapping areas. These areas are shown in Figure 2-2. Area 24 is the whole region (i.e. the area bounded by

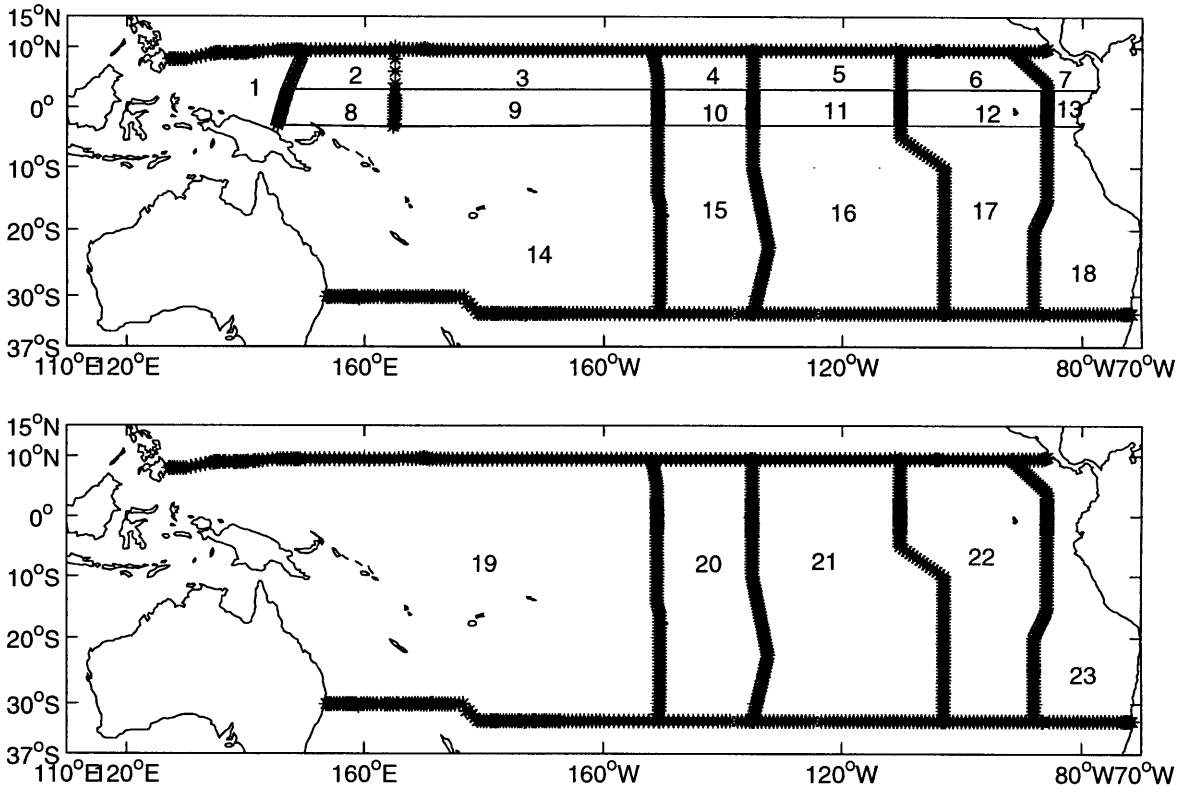

Figure 2-2: Maps showing the areas defined in the model. Area 24 is the whole region bounded by P4, P6 and the two continents

sections P4 and P6 and the continents).

Each area was then divided into 14 layers in the vertical. The bounding isopycnal surfaces were based on those of *Wijffels* [1993] and *Tsimplis et al.* [1998] and are shown in Table 2.1

Layer number	Upper Boundary	Lower Boundary
1	surface	$\sigma_\theta = 23.5$
2	$\sigma_\theta = 23.5$	$\sigma_\theta = 24.5$
3	$\sigma_\theta = 24.5$	$\sigma_\theta = 25.5$
4	$\sigma_\theta = 25.5$	$\sigma_\theta = 26.2$
5	$\sigma_\theta = 26.2$	$\sigma_\theta = 26.7$
6	$\sigma_\theta = 26.7$	$\sigma_\theta = 27.1$
7	$\sigma_\theta = 27.1$	$\sigma_2 = 36.5$
8	$\sigma_2 = 36.5$	$\sigma_2 = 36.75$
9	$\sigma_2 = 36.75$	$\sigma_2 = 36.85$
10	$\sigma_2 = 36.85$	$\sigma_2 = 36.95$
11	$\sigma_2 = 36.95$	$\sigma_4 = 45.81$
12	$\sigma_4 = 45.81$	$\sigma_4 = 45.85$
13	$\sigma_4 = 45.85$	$\sigma_4 = 45.93$
14	$\sigma_4 = 45.93$	bottom
15	surface	bottom

Table 2.1: The labels and bounding pressure surfaces for the model layers

2.2.2 Model Equations

Balance equations for mass, salt and heat may be written for each of the boxes defined and are of the form:

$$\sum_j \sum_q \rho_j(q) C_j(q)(\mathbf{v}_{g_j} + b_j)\delta_j \Delta a_j(q) + \overline{w_B} A \overline{C_B} - \overline{w_T} A \overline{C_T} + \sum_k (T_{Ek})_k = 0 \qquad (2.4)$$

where: j number of station pairs bounding box

q number of standard depths in layer

C temperature or salinity

b reference level velocity

δ ± 1 to define positive direction as into the box

Δa vertical interface area

$\overline{w_B}, \overline{w_T}$ vertical velocity across bottom and top of box

A horizontal area of box

$\overline{C_B}, \overline{C_T}$ mean temperature and salinity over bottom and top of box

k number of Ekman grid points bounding box

and other variables have been previously defined.

For each box, this may be written in vector form as

$$\mathbf{ab} + n = -\gamma \tag{2.5}$$

where $\mathbf{a} = \left(\sum_q \rho_1(q) C_1(q) \delta_1 \Delta a_1(q) \quad \cdots \quad \sum_q \rho_j(q) C_j(q) \delta_j \Delta a_j(q) \quad A\overline{C_B} \quad A\overline{C_T} \right)$

$\mathbf{b} = \left(b_1 \quad b_2 \quad \cdots \quad b_j \quad \overline{w_B} \quad \overline{w_T} \right)^T$

$\gamma = \sum_j \sum_q \rho_j(q) C_j(q) \mathbf{v}_g \delta_j \Delta a_j(q) + \sum_k (T_{Ek})_k$

and n represents noise due to uncertainty in the observations

Writing an equation like this for each box and for each conserved quantity gives a set of simultaneous equations which can be represented as a matrix equation:

$$\mathbf{Ab} + \mathbf{n} = \mathbf{\Gamma} \tag{2.6}$$

There are a variety of methods that can be used to solve such a system. Here, it was decided to use Gauss-Markov estimation which gives an estimate, $\tilde{\mathbf{b}}$, which minimizes the mean square difference between the estimated solution and the true solution (i.e. minimizes $\left\langle \left(\tilde{\mathbf{b}} - \mathbf{b} \right)_i^2 \right\rangle$) The expressions for the solutions are as follows [*Wunsch*, 1996]:

$$\tilde{\mathbf{b}} = \mathbf{R}_{bb} \mathbf{A}^T \left(\mathbf{A} \mathbf{R}_{bb} \mathbf{A}^T + \mathbf{R}_{nn} \right)^{-1} \mathbf{\Gamma} \tag{2.7}$$

$$\tilde{\mathbf{n}} = \left\{ \mathbf{I} - \mathbf{A} \mathbf{R}_{bb} \mathbf{A}^T \left(\mathbf{A} \mathbf{R}_{bb} \mathbf{A}^T + \mathbf{R}_{nn} \right)^{-1} \right\} \mathbf{\Gamma} \tag{2.8}$$

$$\mathbf{P} = \mathbf{R}_{bb} - \mathbf{R}_{bb}\mathbf{A}_T \left(\mathbf{A}\mathbf{R}_{bb}\mathbf{A}^T + \mathbf{R}_{nn}\right)^{-1} \mathbf{A}\mathbf{R}_{bb} \tag{2.9}$$

$$\mathbf{P}_{nn} = \left\{\mathbf{I} - \mathbf{A}\mathbf{R}_{bb}\mathbf{A}^T \left(\mathbf{A}\mathbf{R}_{bb}\mathbf{A}^T + \mathbf{R}_{nn}\right)^{-1}\right\} \times \mathbf{R}_{nn} \left\{\mathbf{I} - \mathbf{A}\mathbf{R}_{bb}\mathbf{A}^T \left(\mathbf{A}\mathbf{R}_{bb}\mathbf{A}^T + \mathbf{R}_{nn}\right)^{-1}\right\} \tag{2.10}$$

$\tilde{\mathbf{b}}$ and $\tilde{\mathbf{n}}$ are the estimated solution (the reference level velocities and vertical velocities) and the model residuals (remaining box imbalances). $\mathbf{P}(=< (\tilde{\mathbf{b}} - \mathbf{b})(\tilde{\mathbf{b}} - \mathbf{b})^T >)$ is the solution uncertainty (i.e. the dispersion of $\tilde{\mathbf{b}}$ about the true solution) and $\mathbf{P}_{nn}(=< (\tilde{\mathbf{n}} - \mathbf{n})(\tilde{\mathbf{n}} - \mathbf{n})^T >)$ is the uncertainty of the residuals. $\mathbf{R}_{bb}$ and $\mathbf{R}_{nn}$ are described in the next section.

2.2.3 Estimated variances

Gauss-Markov estimation requires the *a priori* specification of the expected dispersion of the solution ($\mathbf{R}_{bb} =< \mathbf{b}\mathbf{b}^T >$) and the residuals ($\mathbf{R}_{nn} =< \mathbf{n}\mathbf{n}^T >$). Physically, the diagonals of these matrices are the expected order of magnitude of the reference level and vertical velocities and the error to within which a box is considered to be in balance. $\mathbf{R}_{bb}$ and $\mathbf{R}_{nn}$ were both initially defined as diagonal matrices and so implicitly include the assumption that there is no correlation in noise between station pairs or between boxes. A typical set of variances, based on those which have been used in prior work was used as a starting point for finding an accurate set of constraints for this particular problem. These are summarised in Table 2.2.3. In preliminary models, the only change made to these constraints was that variance of the reference level velocities within 3^o of the equator were set to zero since the LADCP data is absolute velocity.

2.2.4 Initial imbalances

Figure 2-3b shows the initial layer and top to bottom imbalance in each of the areas.

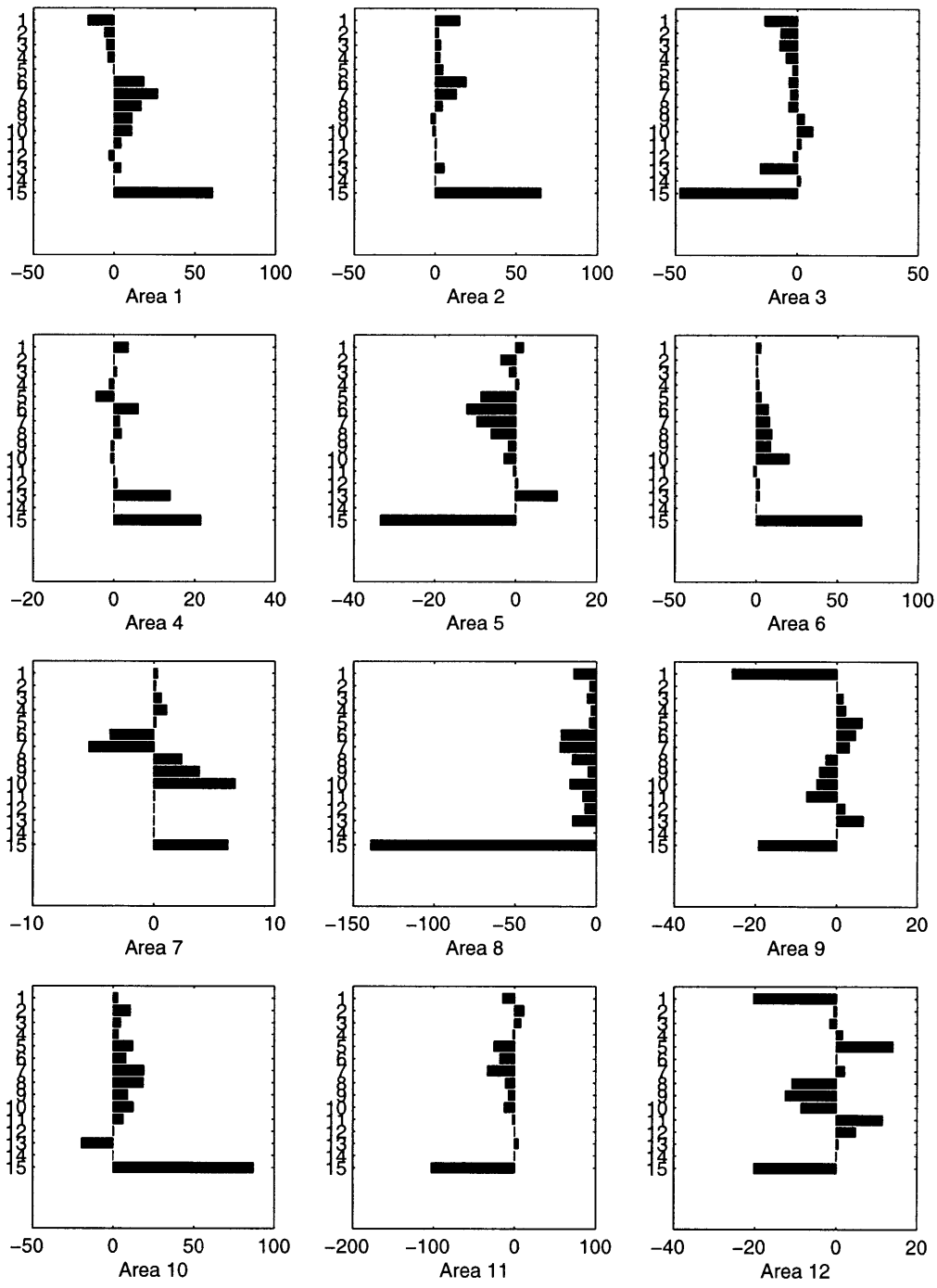

Figure 2-3a: Initial imbalances (in Sv) in each layer and top to bottom (layer 15) for areas 1–12.

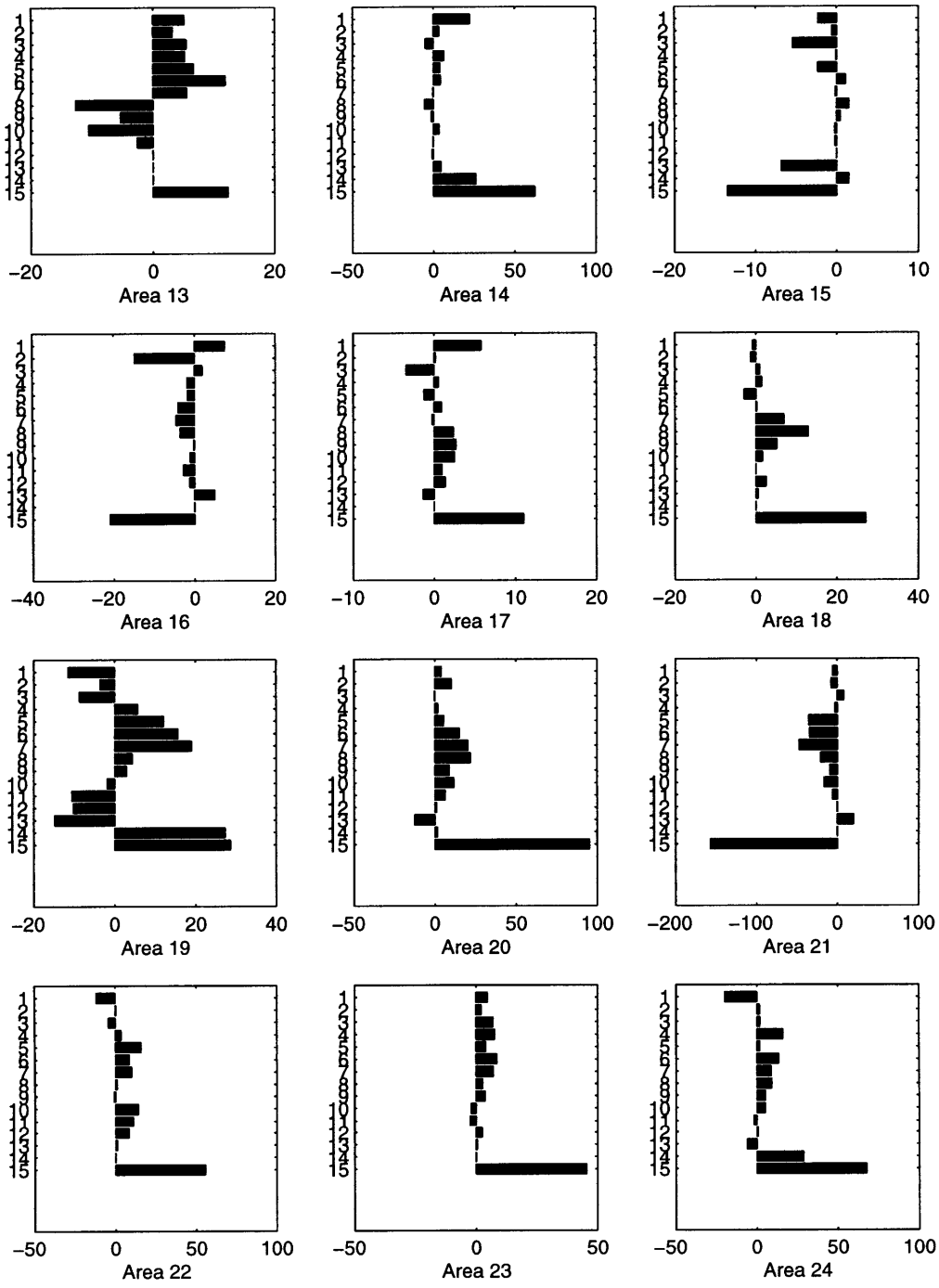

Figure 2-3b: As for Figure 2-3a but for areas 13–24

Reference level velocities		$\pm 1 cms^{-1}$
Vertical velocities		$\pm 1 \times 10^{-4} cms^{-1}$
box imbalances		$\pm 1 Sv$
except	boxes in contact with surface	$\pm 2 Sv$

Table 2.2: Summary of constraints typically applied to inverse problems

It can be seen that there are only a few boxes in which the constraints are met by the relative velocity field alone. Part of this imbalance arises from errors at the points where the hydrographic sections cross in mid-ocean. Seasonal variability and the presence of eddies can cause large discrepancies. In most areas, the imbalance is distributed through the water column, although a small imbalance in each layer can cumulatively give a large top to bottom imbalance. However, in area 9 the imbalance is dominantly in the surface layer. The imbalances in areas 20 and 21 have a similar structure but opposite sign suggesting that it is the boundary between these two areas (P17) that is dominating the balance in these regions. It would appear that this is mostly a result of transports in the equatorial region since the imbalances in areas 10 and 11 also show a similar structure with opposite signs but areas 4 and 5 and areas 15 and 16 do not.

2.3 Model solutions

Several sets of constraints were tested to attempt to find a solution that may be considered to be consistent with the specified statistics. One definition of consistent may be that all the unknowns must come within the specified constraints. However, if the initial variances are considered to be one standard deviation then a consistent solution may be one for which more than 67% of the unknowns are found to be within the specified limits. The acceptability of a solution may also depend on which boxes

do not meet the constraints, since it would be anticipated that larger areas should be closer to balance. For example, a solution for which 80% of the boxes are within the specified constraints may be accepted if all boxes in areas 19-24 are in balance whilst those in smaller areas are less well balanced, but may be rejected if the larger boxes are outside the constraints but more of the smaller areas meet the constraint. Similarly, poorly balanced equatorial boxes maybe deemed more acceptable than poor balance in other boxes due to the highly variable and energetic flow in the equatorial zone.

2.3.1 Simplified model

As a first check, a simplified model consisting only of sections P4 and P6 was constructed to see if a reasonable solution could be found for the region as a whole. Figure 2-4 shows the solution using the 'typical' constraints shown in Table 2.2.3. It can be seen that all boxes balance to within the specified constraints, except level 6 which has a residual of -1.22 Sv, but this is still an acceptable residual. The cross-isopycnal velocity for the lowest isopycnal ($\sigma_\theta = 45.93$) is the only velocity to fall outside the constraints but the cross-isopycnal transports all appear to be a reasonable order of magnitude given the size of the region and that strong upwelling in the upper layers would be anticipated in the equatorial zone.

A solution was also found in which the cross-isopycnal velocities were constrained to be $1 \times 10^{-5} cms^{-1}$ (other constraints were the same as in the previous case) and this is shown in Figure 2-5. In this case, both the surface layer and layer 6 are not quite in balance with residuals of 3.63 Sv and -1.26 Sv (compared with the specified 2 Sv and 1 Sv). Only the transfer across the lowest isopycnal is strongly affected and this is now close to zero compared with about $8Sv$ in the previous solution. The only obvious difference in the reference level velocities for the two solutions is the increased

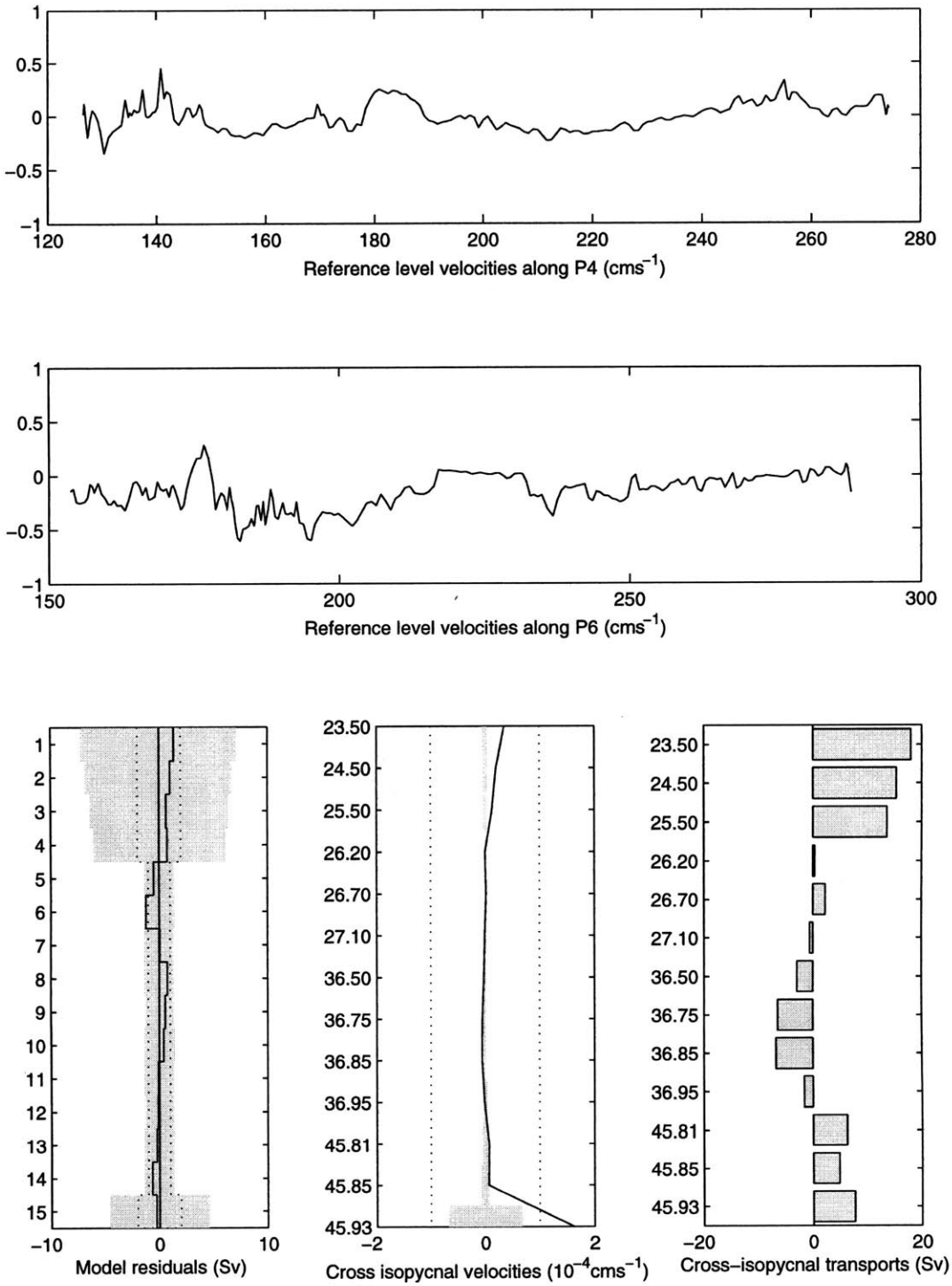

Figure 2-4: Model solution for the simplified model using typical constraints. Dotted lines are the *a priori* specified variances and the shaded region on the lower left and middle panels is the solution uncertainty

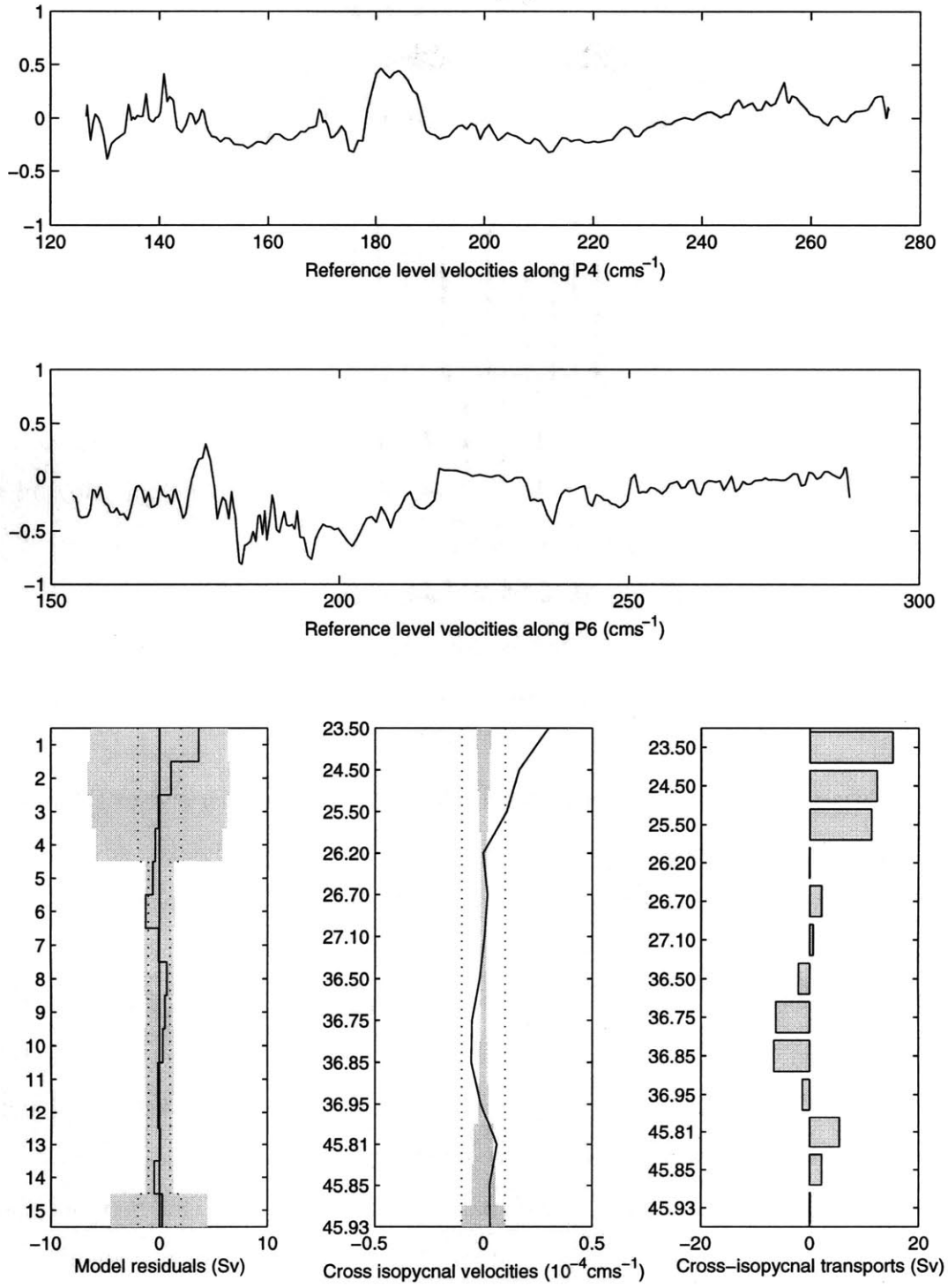

Figure 2-5: As for Figure 2-4 but using modified constraints.

velocities on P4 around 180°W, but the magnitude of these is still well within the constraints.

2.3.2 Full model

Having achieved reasonable solutions for the single area model, solutions of the full model with 24 areas were investigated.

Figure 2-6a – 2-6i show the solution for the model using the set of typical constraints summarised in Table 2.2.3. In this case, 44% of model residuals, 80% of the reference level velocities and 45% of the cross-isopycnal velocities were within the specified constraints. This solution is clearly not consistent with the specified statistics since not even 2/3 of the estimates are within the expected bounds. However, examination of this solution may give an indication of which constraints should be modified.

The largest reference level velocities are found at the western end of P4 and this may be related to the large uncertainty associated with Box 1 due to the Indonesian Throughflow. Also, on P4 around 110°W, which is close to the intersection of P4 with P18, and on P6 between around 130°W (close to P17) and 110°W (close to P18) there are clusters of large velocities. Over the whole region (i.e. area 24), balance is fairly closely achieved but in the smaller areas, fewer layers are in balance. This is to be expected, if no systematic errors are present in the data, it is more likely that balance would be achieved over a larger region. Many of the cross-isopycnal transports appear to be rather large (greater than 10 Sv) particularly in area 11. This may be related to the strong box balance constraints rather than the specified magnitude of w.

The model constraints were relaxed and another solution found. The box balance constraints were such that in areas 19 - 24, boxes were required to balance to within 2 Sv and to within 3 Sv for boxes in contact with the surface. The constraints

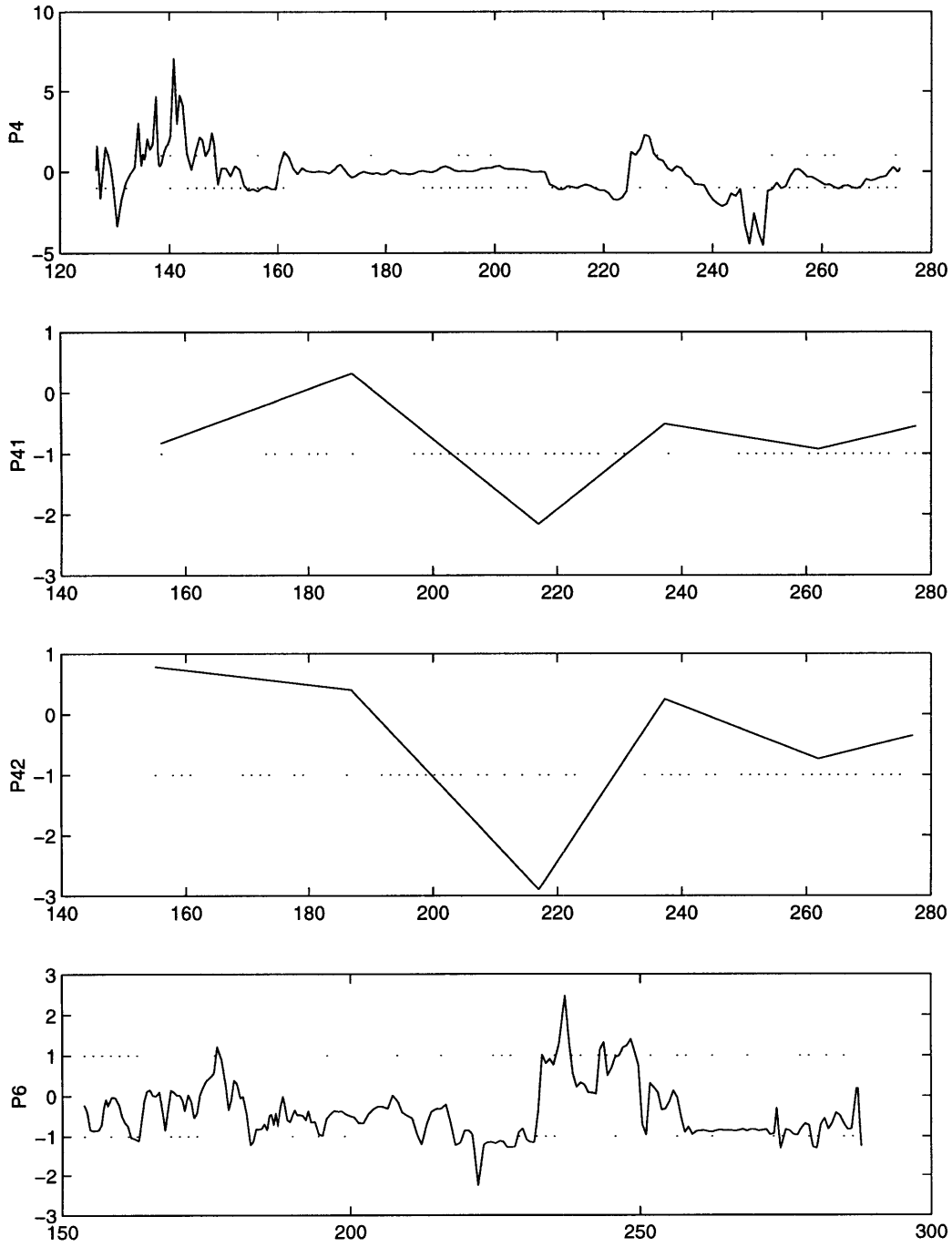

Figure 2-6a: Reference level velocities in cms^{-1} along sections (from the top) P4, P41, P42 and P6 for full model using typical constraints. The dotted lines are the specified variances.

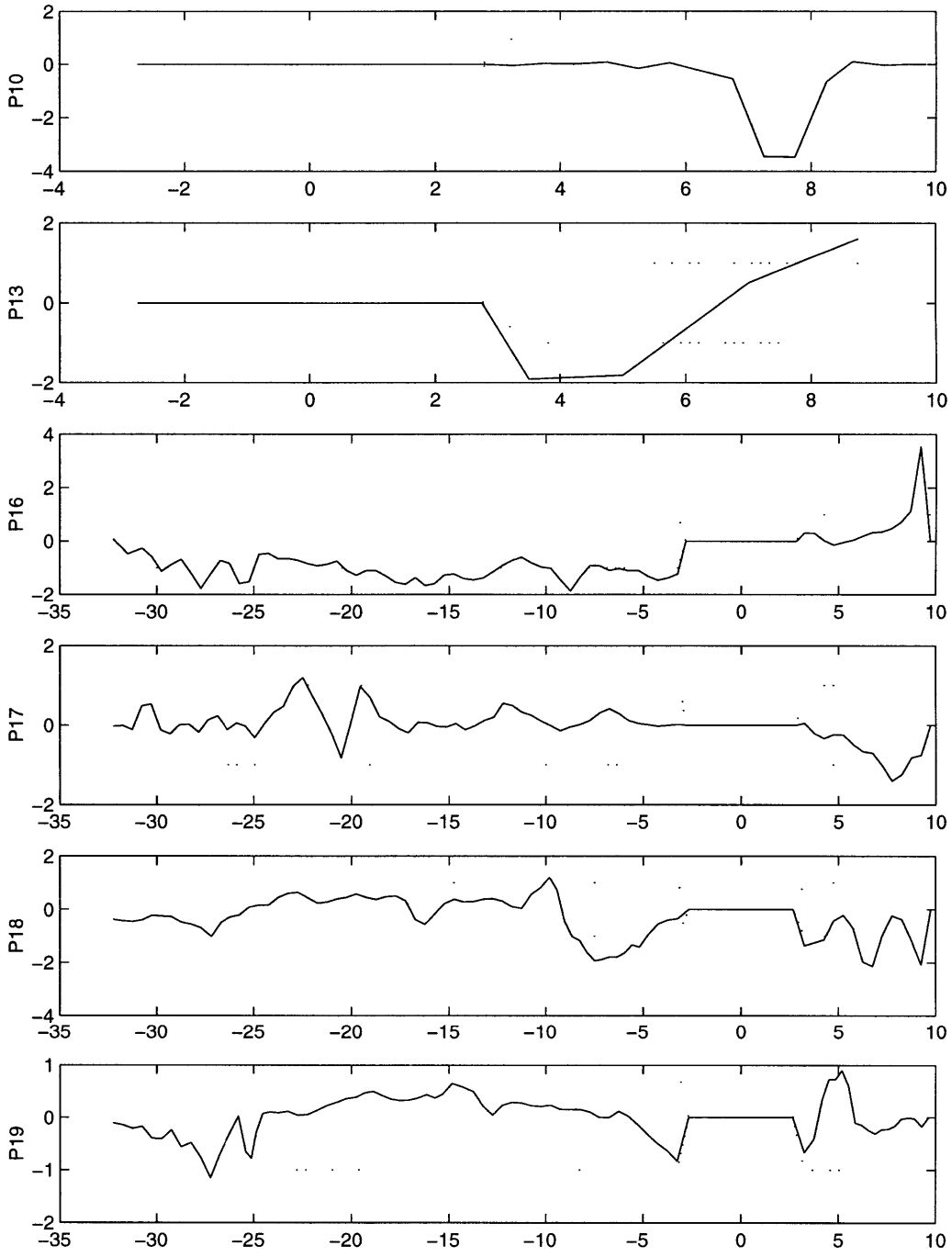

Figure 2-6b: As for figure 2-6a but for sections (from the top) P10, P13, P16, P17, P18 and P19

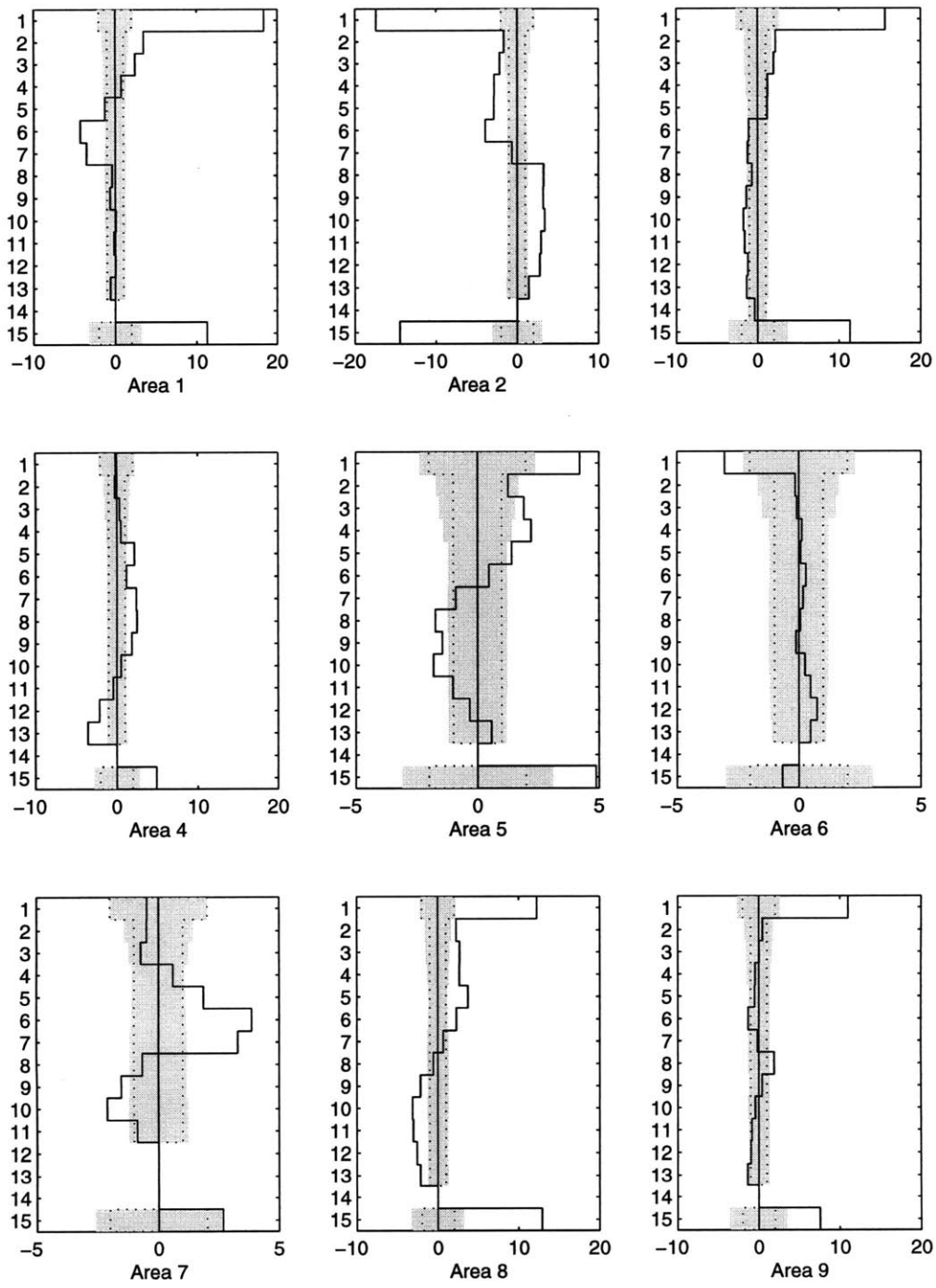

Figure 2-6c: Model residual in Sv for areas 1–9 from full model using typical constraints. The solid lines are the model residuals; the dotted lines are the *a priori* specified variances and the shaded areas are the residual uncertainties (the square root of the diagonal elements of $\mathbf{P}_{nn}$).

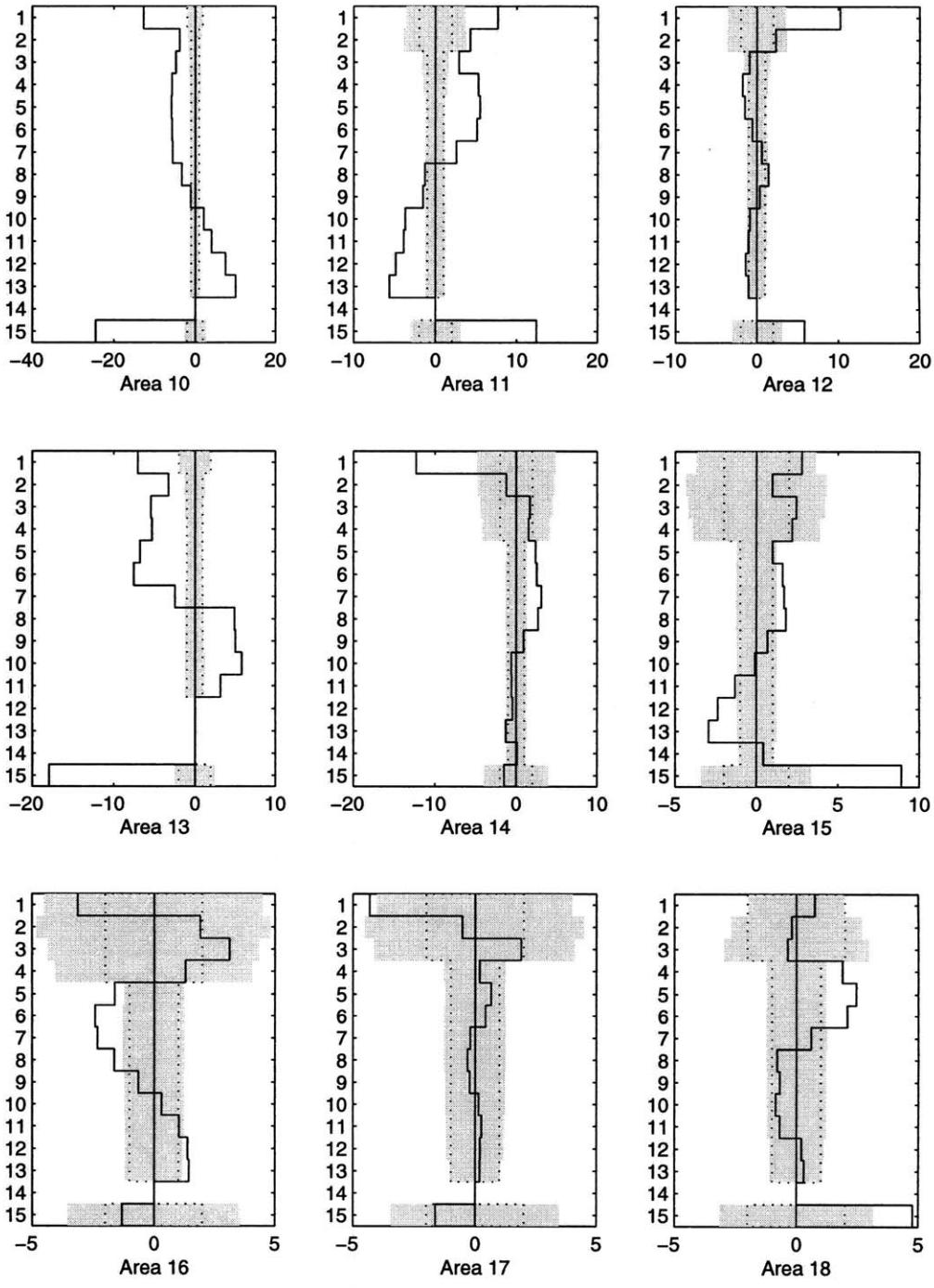

Figure 2-6d: As for Figure 2-6c but for areas 10–18

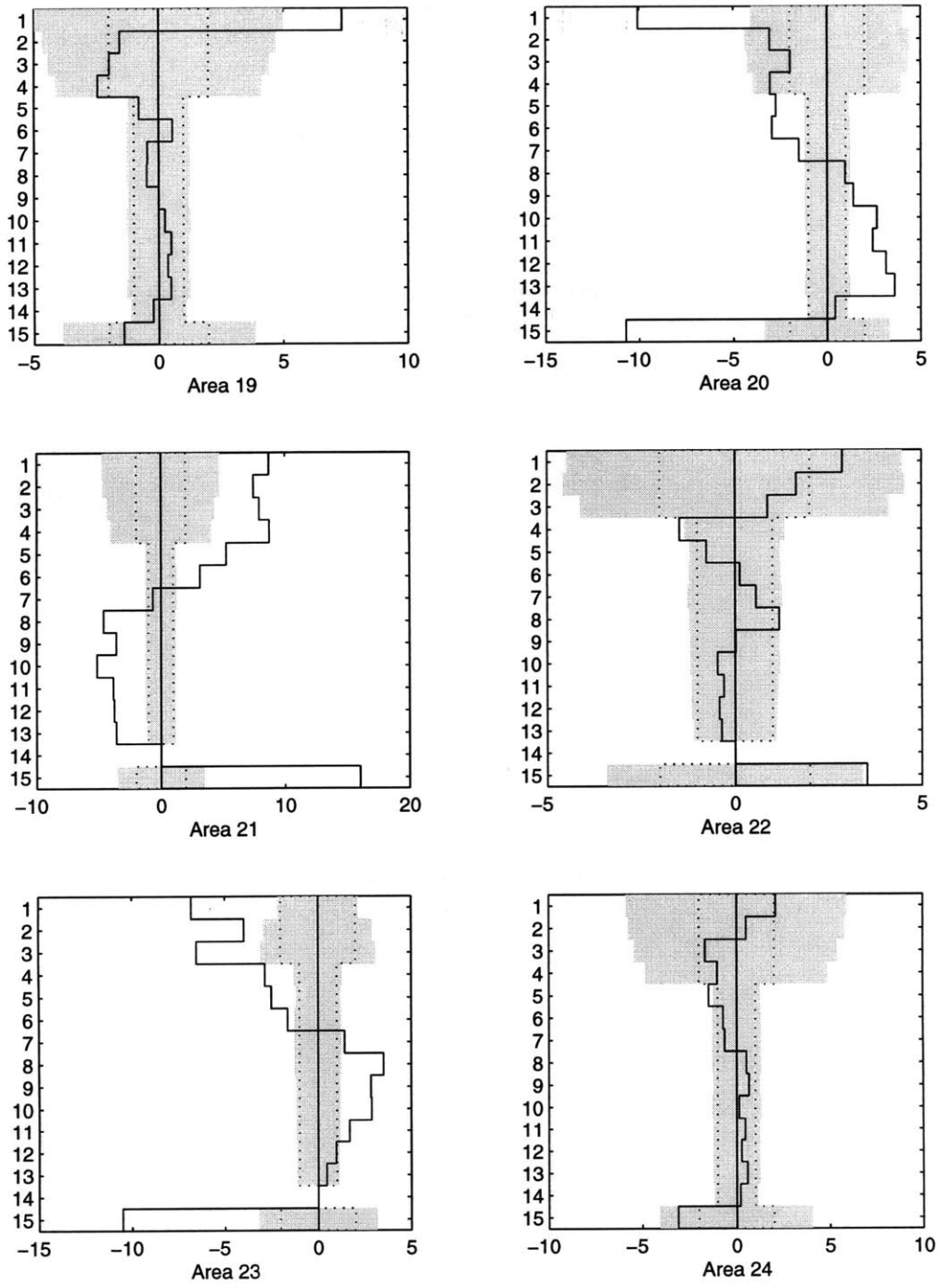

Figure 2-6e: As for Figure 2-6c but for areas 19–24

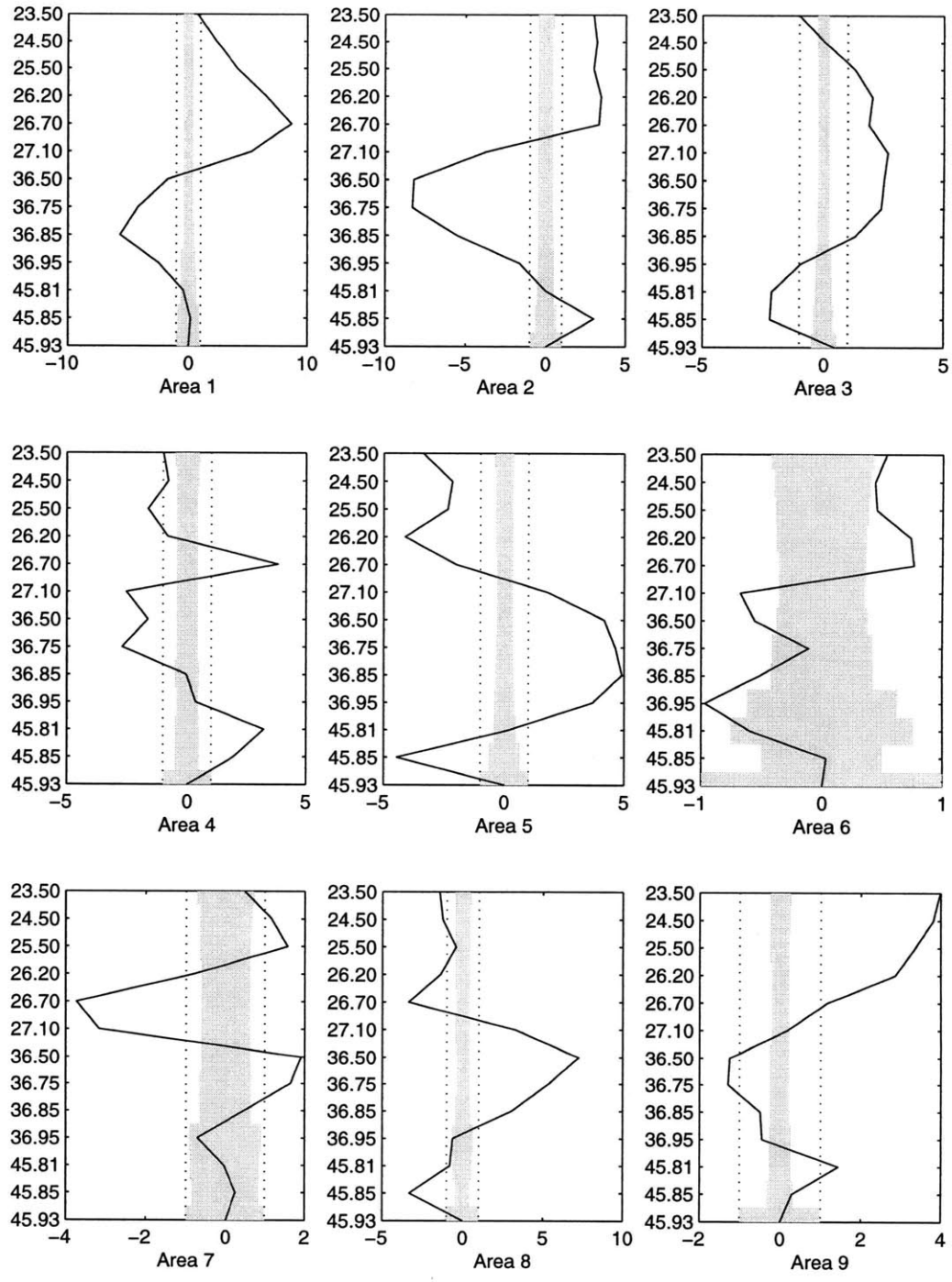

Figure 2-6f: Cross-isopycnal velocities in $10^{-4} cms^{-1}$ for areas 1–9 from full model using typical constraints. The solid lines are the vertical velocities; the dotted lines are the *a priori* specified variances and the shaded regions are the solution uncertainties (the square root of the diagonal elements of $\mathbf{P}_{xx}$).

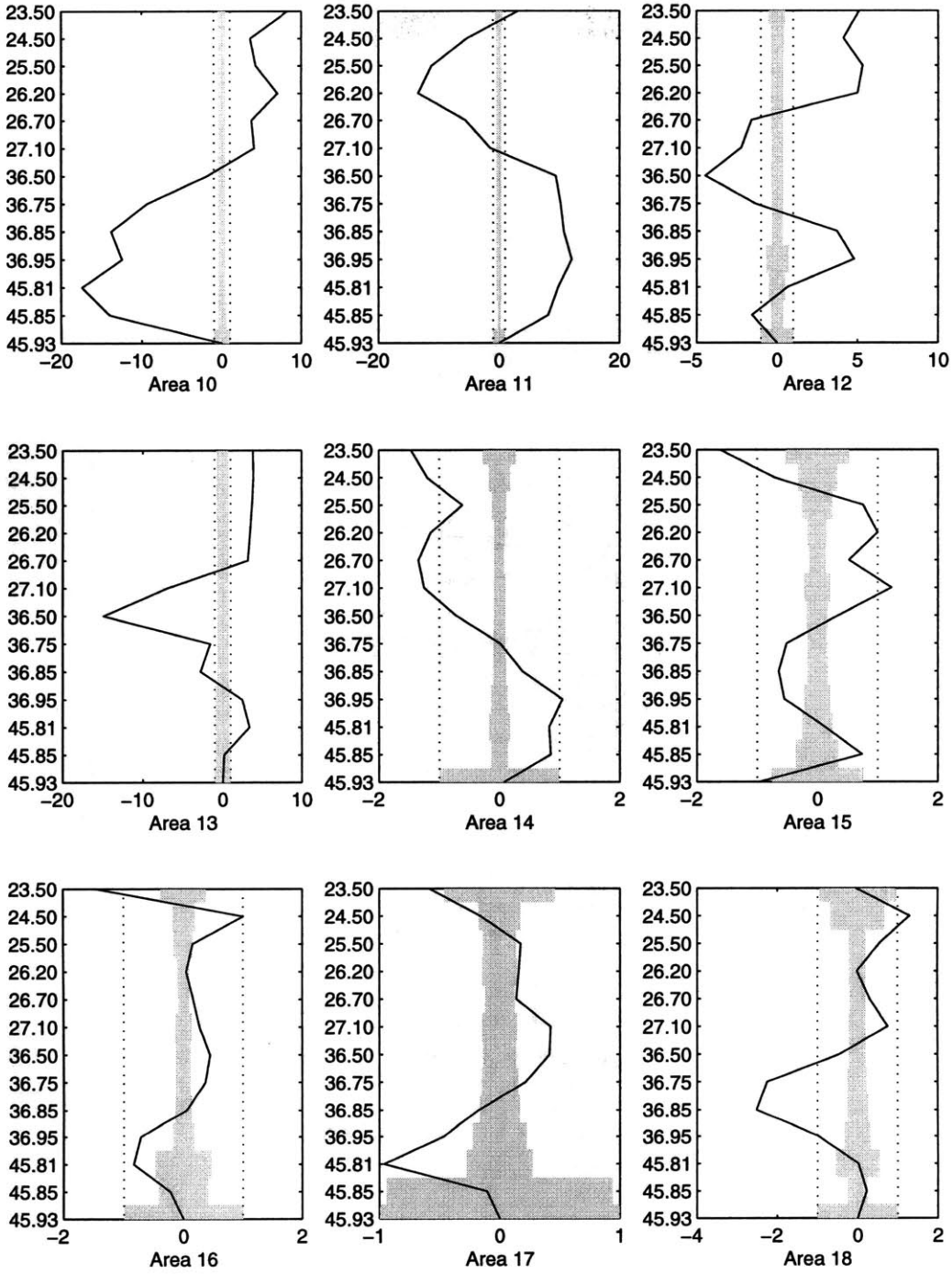

Figure 2-6g: As for figure 2-6f but for areas 10–18.

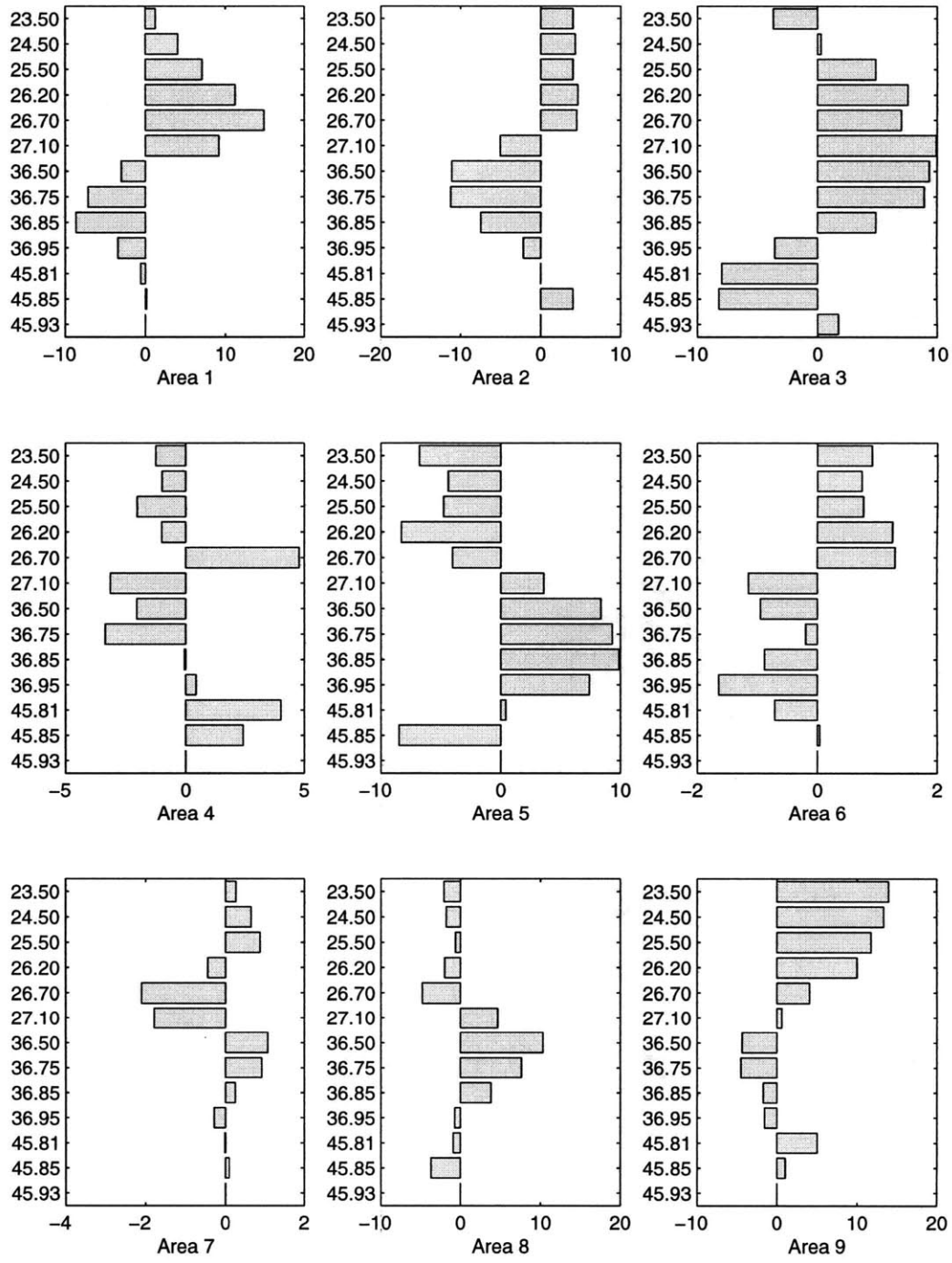

Figure 2-6h: Cross-isopycnal transports in Sv for areas 1–9 from full model using typical constraints.

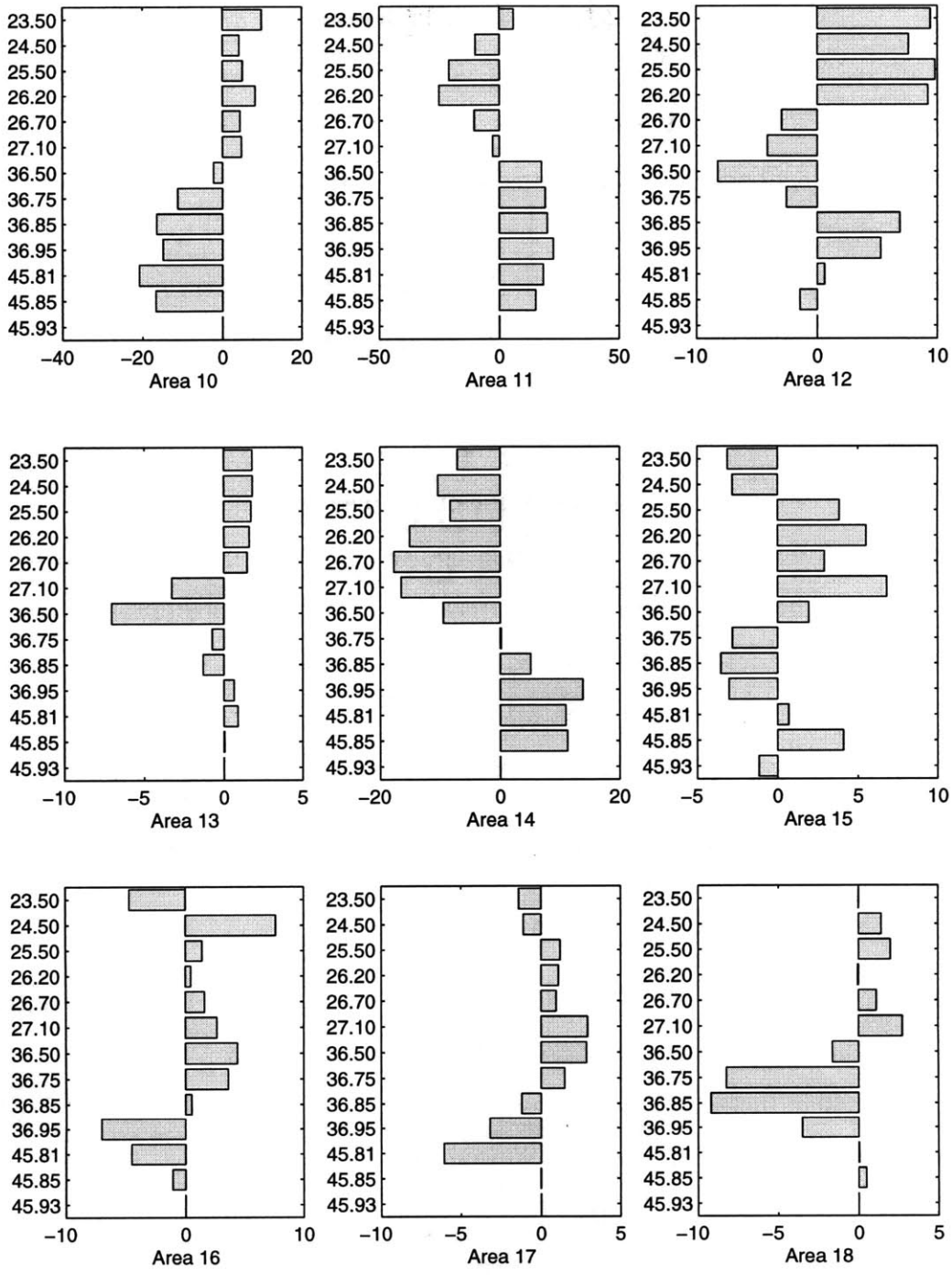

Figure 2-6i: As for Figure 2-6h but for areas 10–18

were relaxed still further for areas 1-18, with balance required to within 5 Sv for each box and 10 Sv for those boxes in contact with the surface. The variance of the cross-isopycnal velocities was increased to $5 \times 10^{-4} cms^{-1}$ for most layers and to $5 \times 10^{-3} cms^{-1}$ for the upper five layers in the equatorial zone. This was done since upwelling is typically much stronger in the equatorial region as a result of the Ekman divergence. In this solution, 84% of model residuals, 99% of reference level velocities and 87% of cross-isopycnal velocities were within the specified range. The solution is shown in Figures 2-7a – 2-7i—these are the same as for Figures 2-6a–2-6i but with the modified constraints. Whilst some of the reference level velocities are outside the specified range, none are of an unacceptable size: the maximum magnitude is 1.48 cms^{-1}. The balance achieved in areas 1-18 is now much improved but many layers in areas 20, 21 and 23 have residuals larger than those specified. It may be that given that this is one-time data from a highly variable region that this is the best that can be achieved. The cross-isopycnal velocities are all of an appropriate order of magnitude.

2.3.3 Horizontal Circulation

Simple circulation diagrams showing the transport across each of the section segments were constructed for three layers. These layers were defined as:

Thermocline: $\sigma_\theta < 26.7$ (model layers 1–5)

Intermediate: $\sigma_\theta > 26.7$; $\sigma_2 < 36.95$ (model layers 6–10)

Deep: $\sigma_2 > 36.95$ (model layers 11-14)

The transports shown should be considered as an indication of the relative size of the transports as errors on some sections may be large. This is discussed further below.

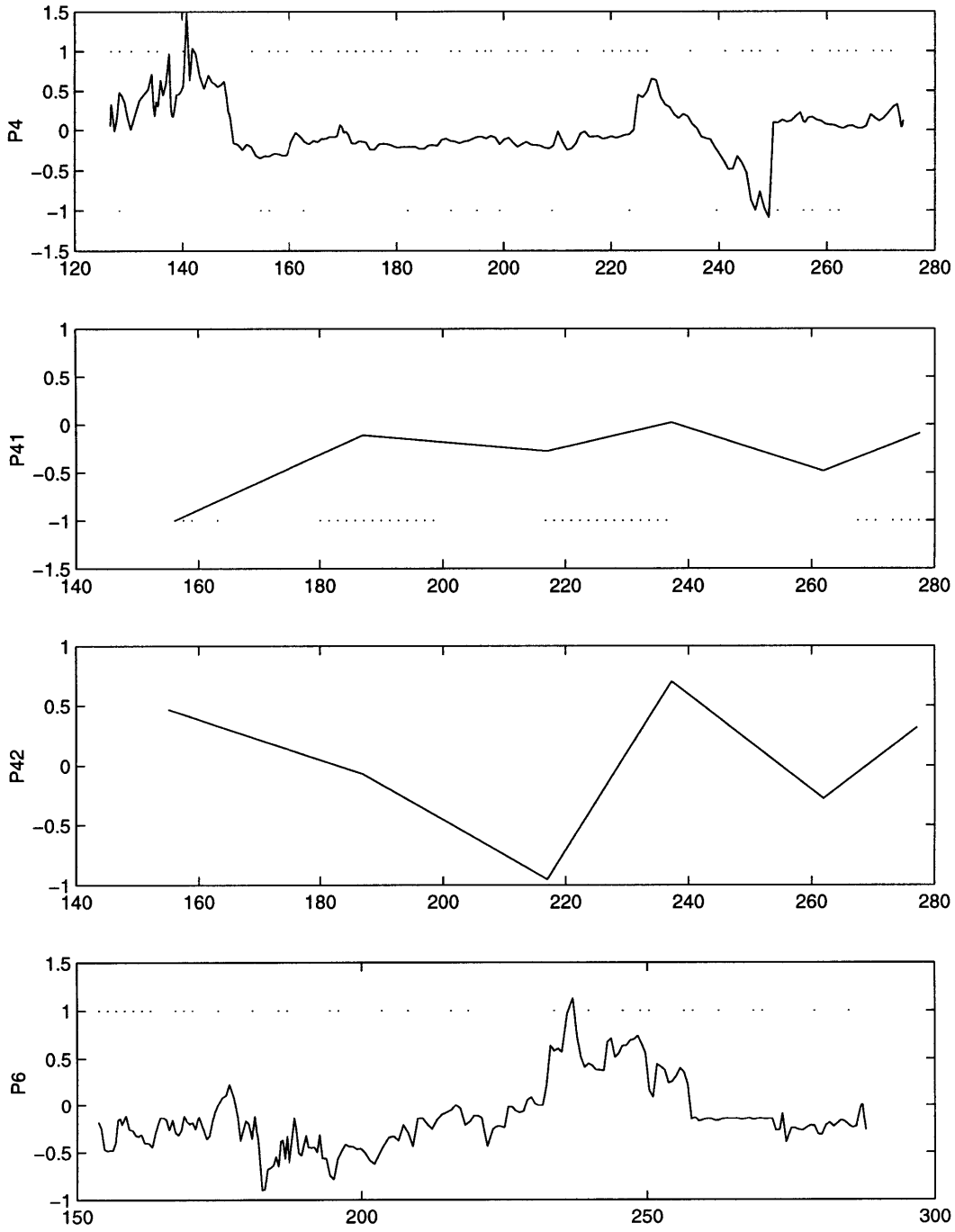

Figure 2-7a: Reference level velocities along zonal sections

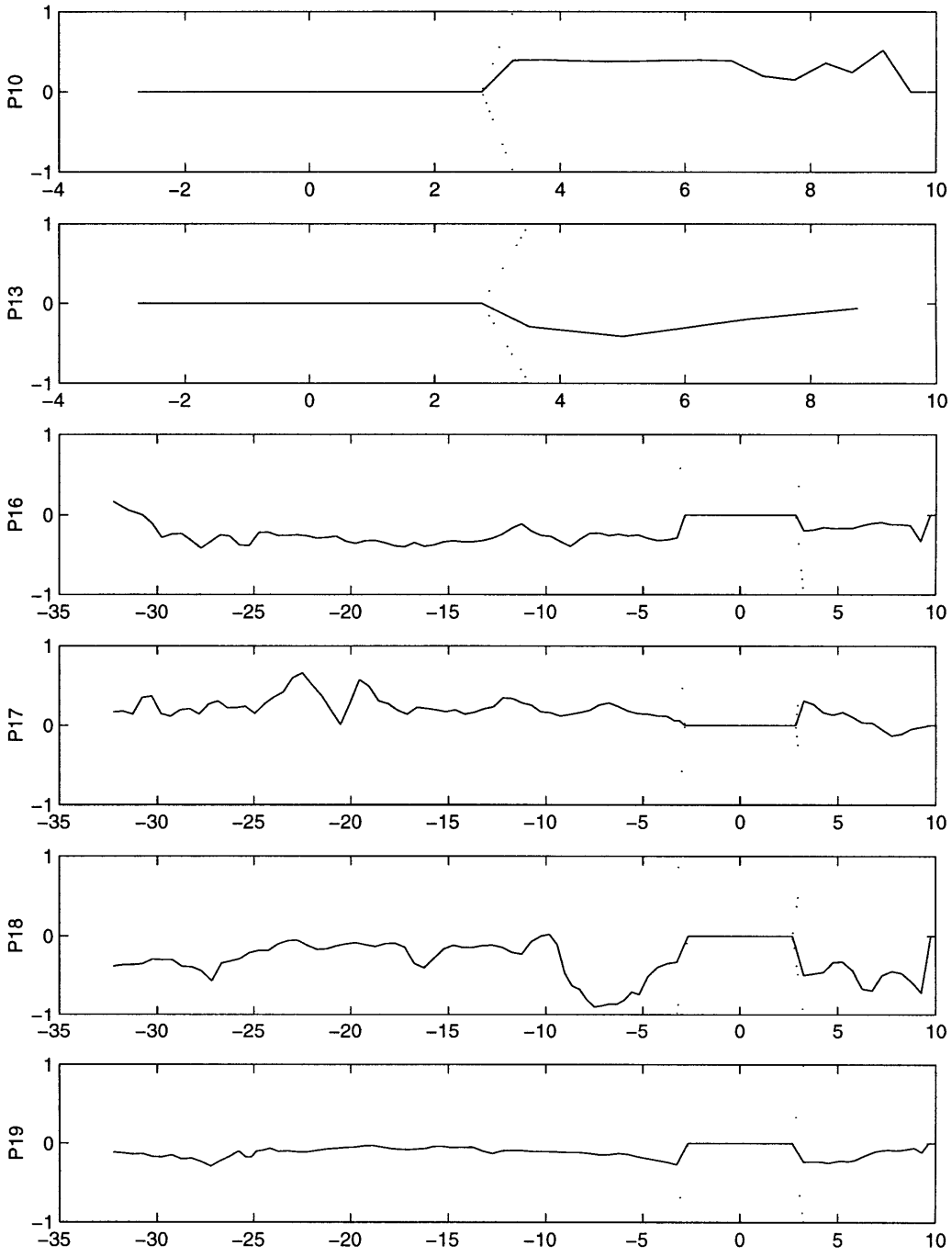

Figure 2-7b: Reference level velocities along meridional sections

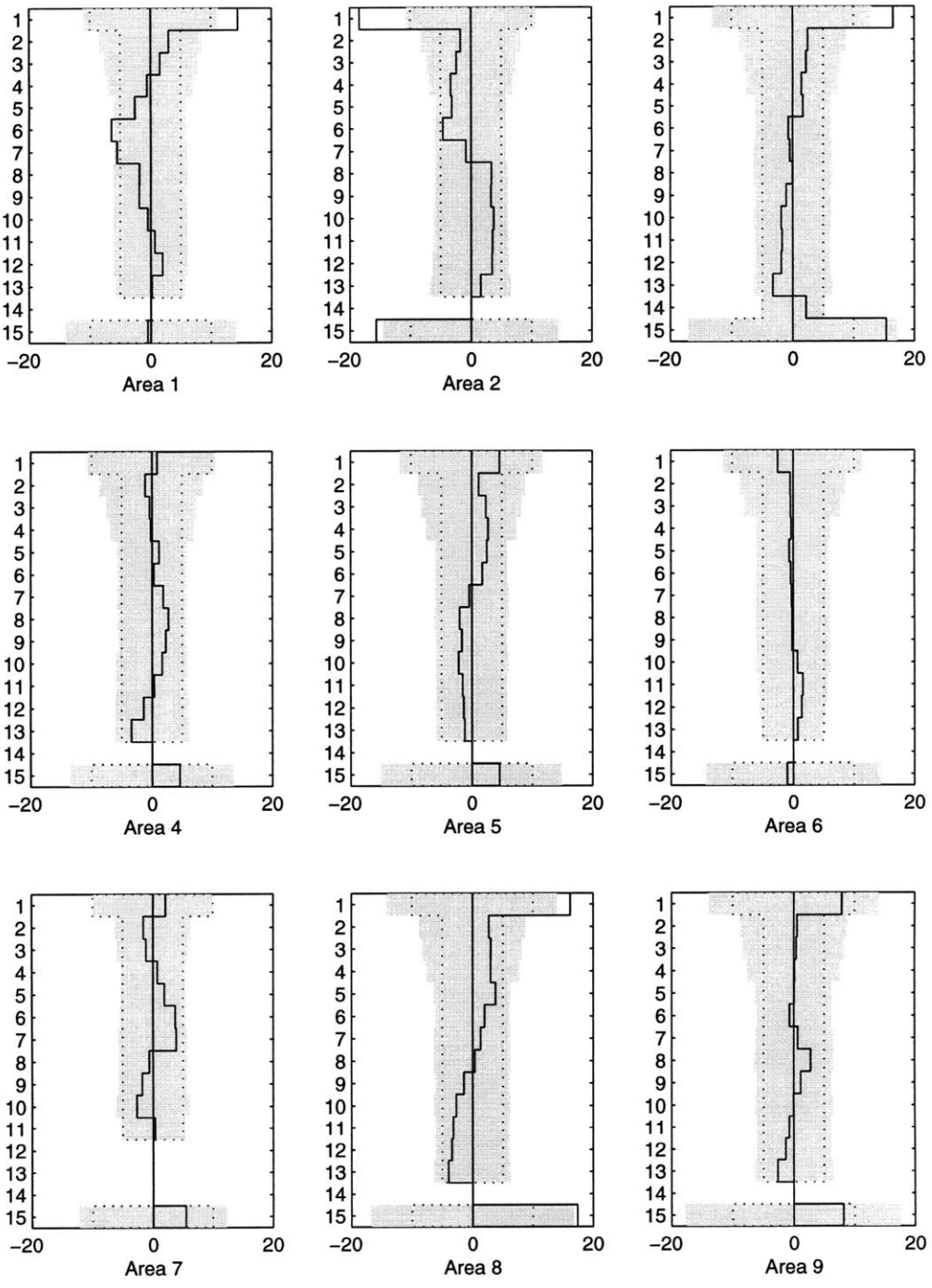

Figure 2-7c: Model residuals in areas 1–9

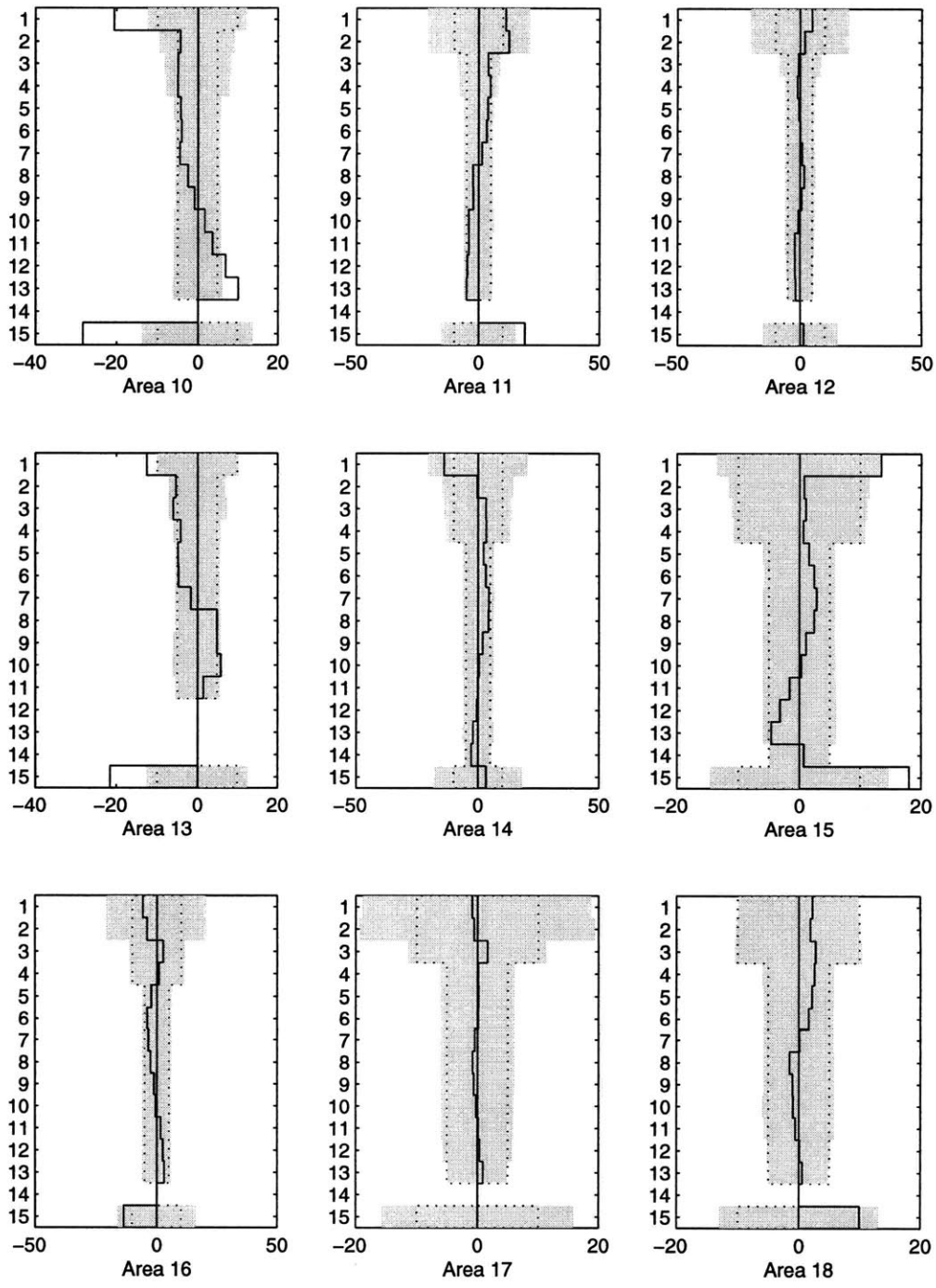

Figure 2-7d: Model residuals in areas 10–18

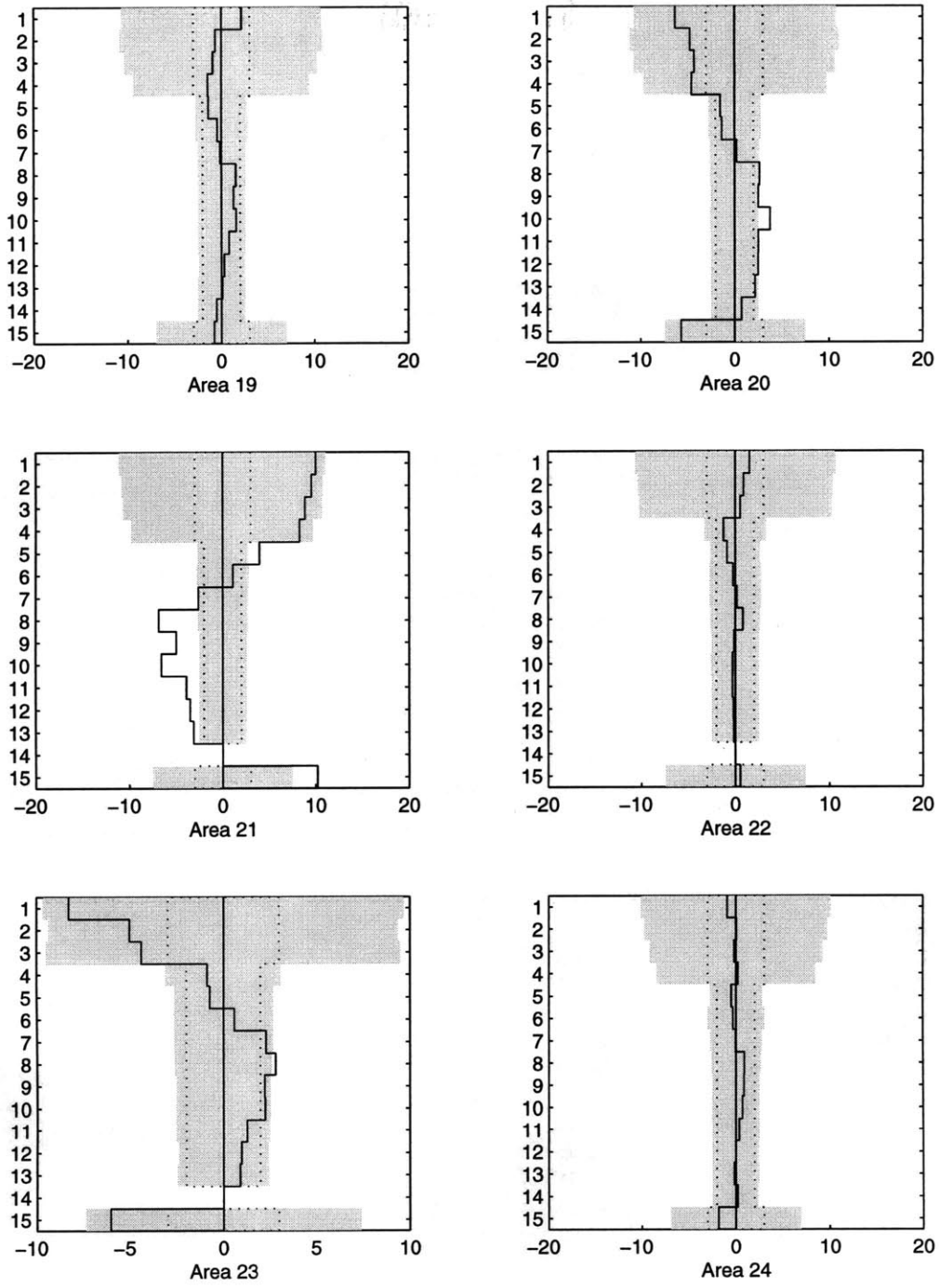

Figure 2-7e: Model residuals in areas 19–24

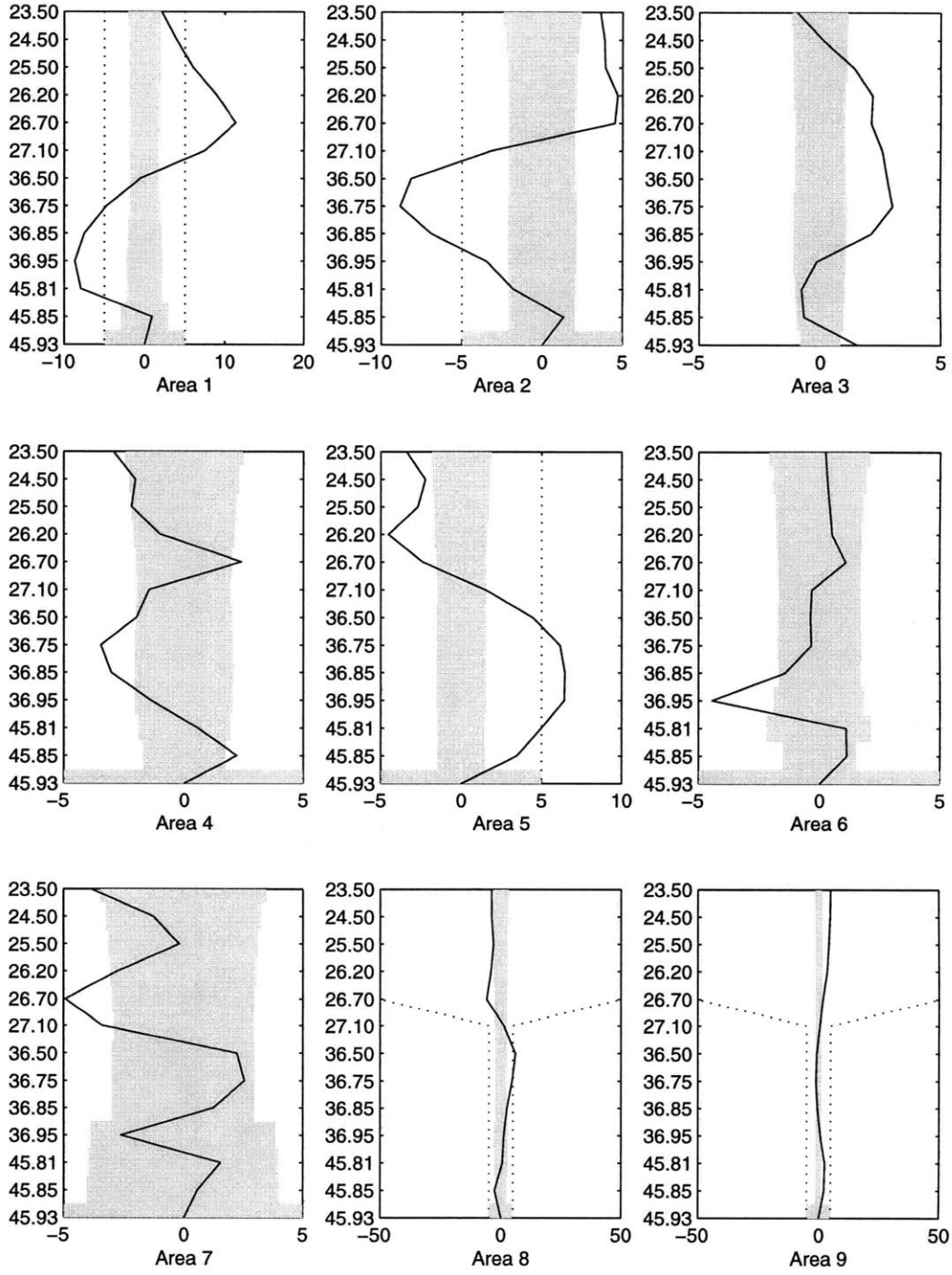

Figure 2-7f: Vertical velocities in areas 1–9

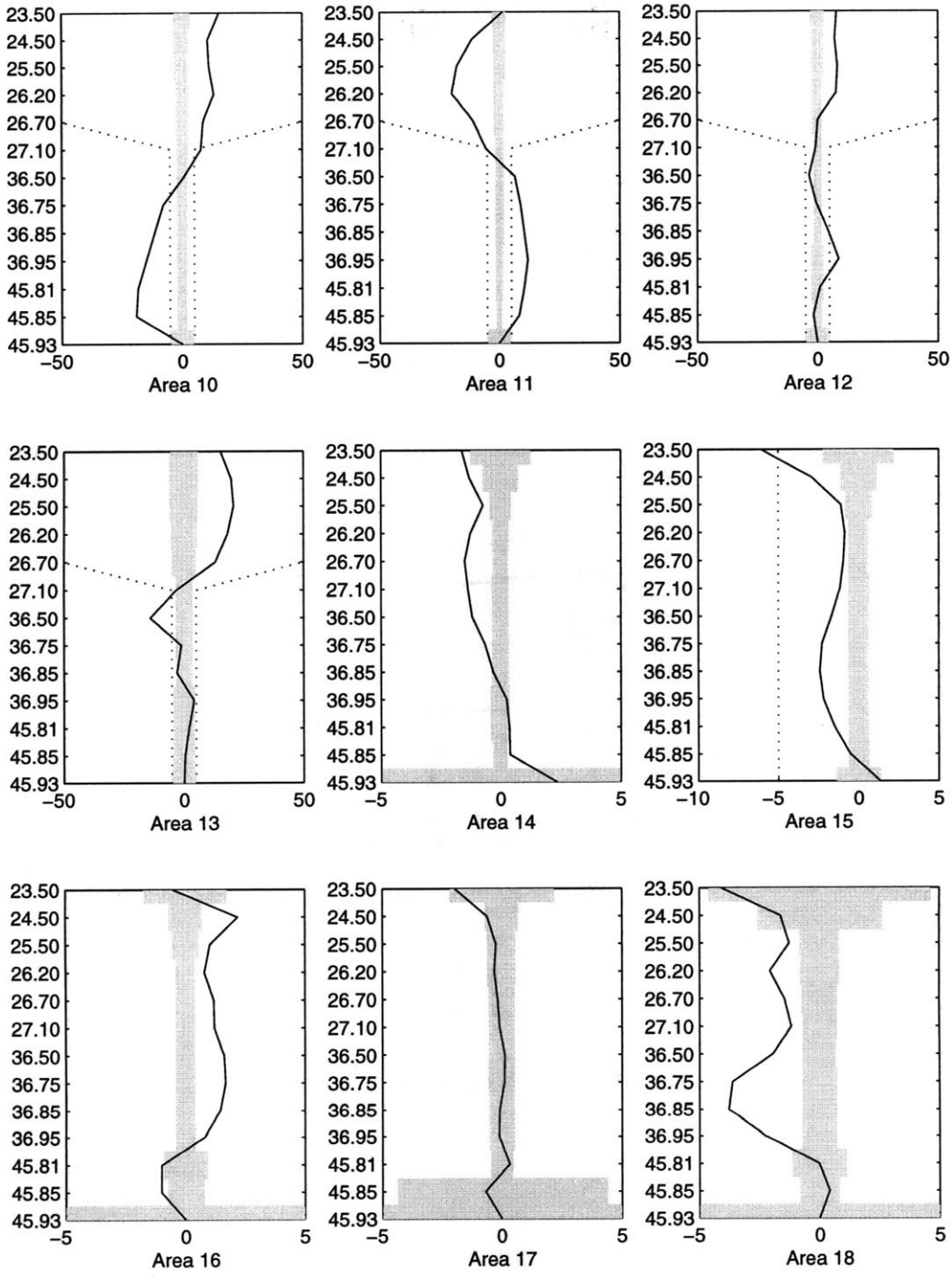

Figure 2-7g: Vertical velocities in areas 10–18

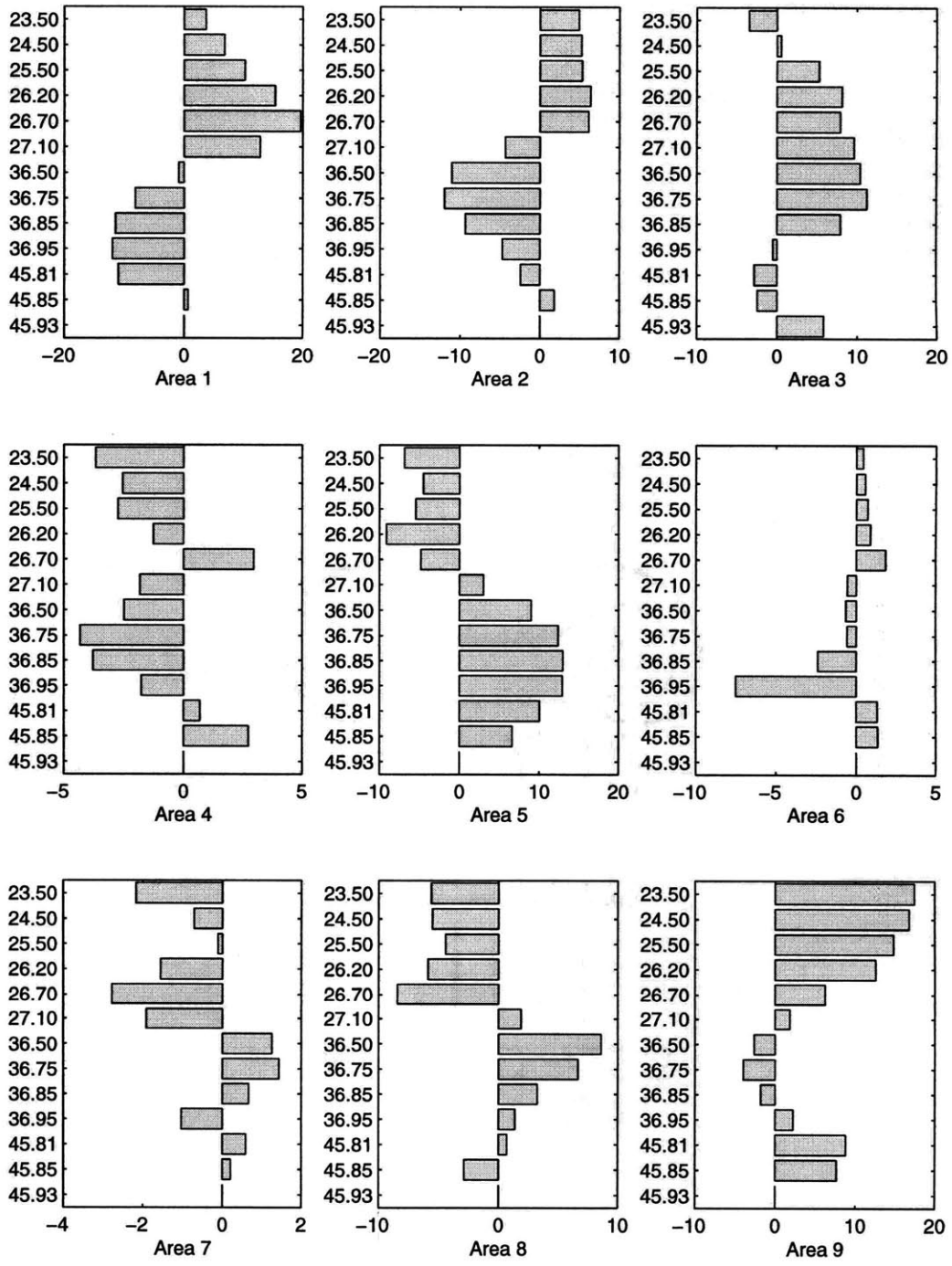

Figure 2-7h: Cross-isopycnal transports in areas 1–9

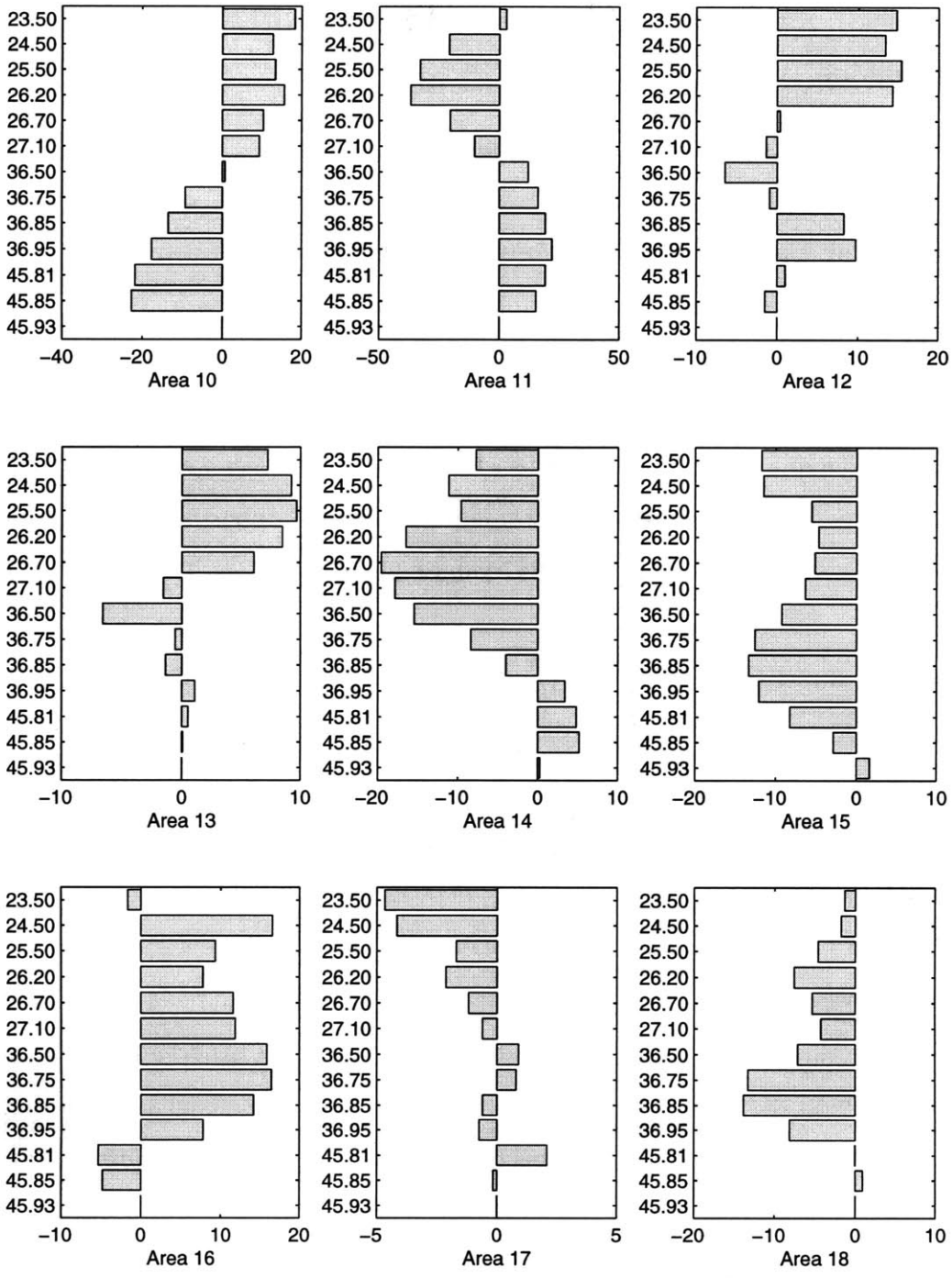

Figure 2-7i: Cross-isopycnal transports in areas 10–18

Thermocline

The transport across each of the section segments in the thermocline are shown in Figure 2-8.

In general, the large-scale circulation shows the expected features. In the equatorial boxes, there is eastward transport which is consistent with the presence of a strong equatorial undercurrent (EUC). The exception to this is across the equatorial segment of P16 where the transport is westward. This reversal may occur because the EUC is anomalously weak on this section or because other westward currents are unusually strong. Figure 2-9 shows the currents in the upper 500m in the equatorial zone across P16 with those on P17 shown for comparison. On the P16 section, the EUC is of about the expected order of magnitude but more significantly, the South Equatorial Current (SEC), is strong beneath the EUC between the equator and 3°N. This would account for the anomalous westward thermocline transport on this section.

In the northern zone (areas 1–7), the flow is also mostly eastward which is consistent with the expected transport of the North Equatorial Counter Current (NECC). The general pattern of northward flow across the eastern parts of P4 and southward across the western part fits with the idea of water being recirculated between the NECC and the westward North Equatorial Current (NEC) north of 10°N. In the southern region (boxes 14–18), the westward flow across the zonal sections, together with the northward transport across the eastern part of P6 and southward transport across the western part is consistent with the sense of the subtropical gyre.

The Ekman component of the transports is shown separately in Figure 2-10. The meridional Ekman transports close to the equator (i.e. on sections P4, P41 and P42) are 1–2 orders of magnitude larger than those across P6 showing how much more important Ekman transport is in the equatorial regions compared with subtropical

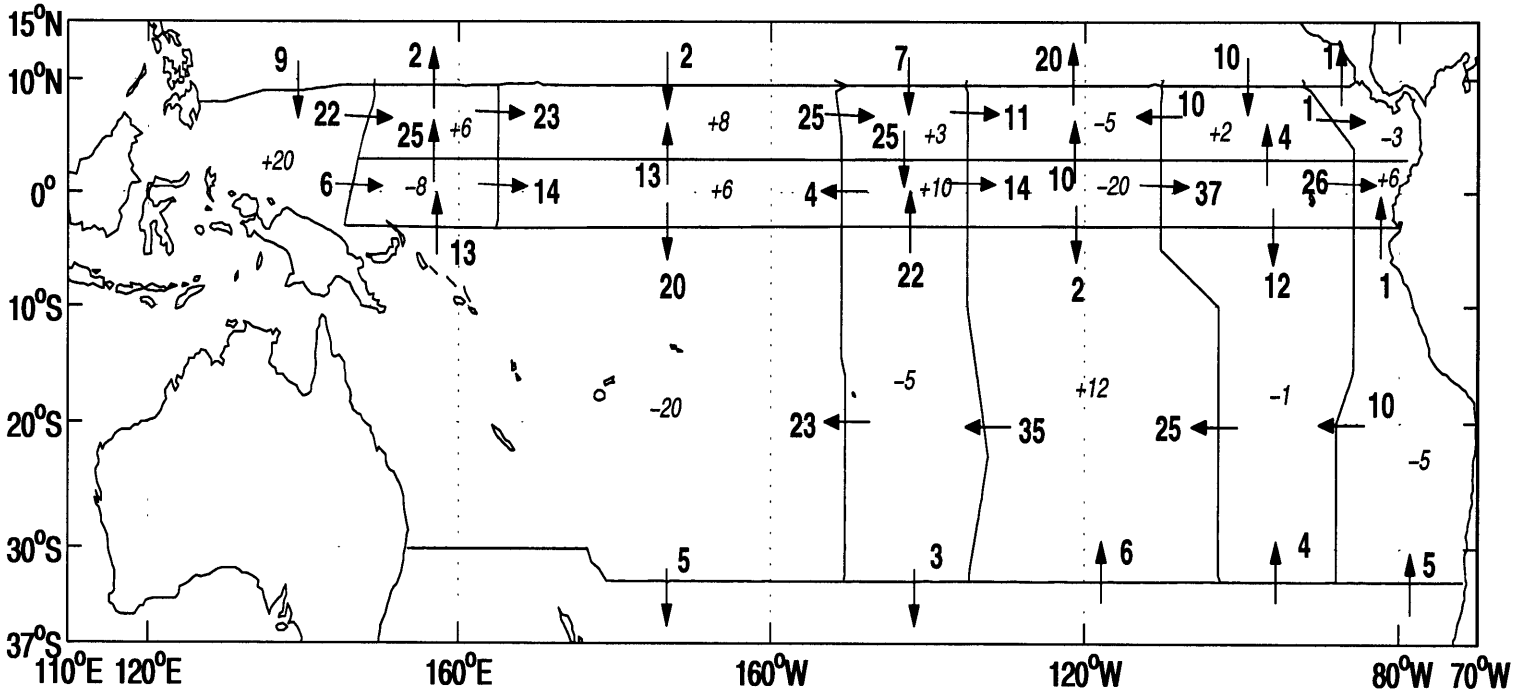

Figure 2-8: Transport in Sv in the thermocline layer. The bold numbers close to the arrows are the approximate magnitude of the transport in the direction of the arrow. The smaller, italic numbers are the approximate upwelling through the base of the layer. Positive numbers are upward *into* the layer.

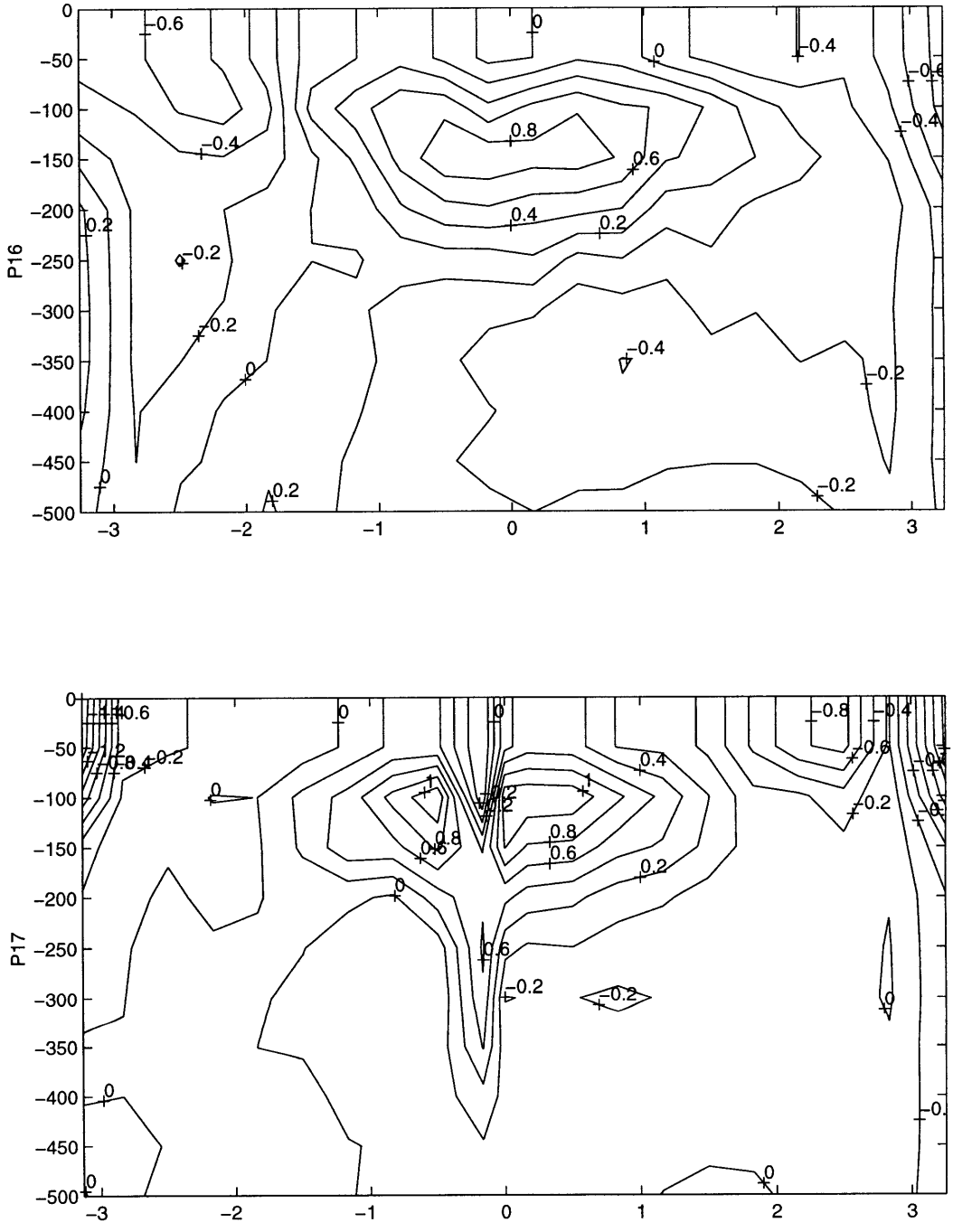

Figure 2-9: Comparison of the currents in the upper equatorial region of sections P16 (upper panel) and P17 (lower panel). The velocities shown are in ms^{-1}.

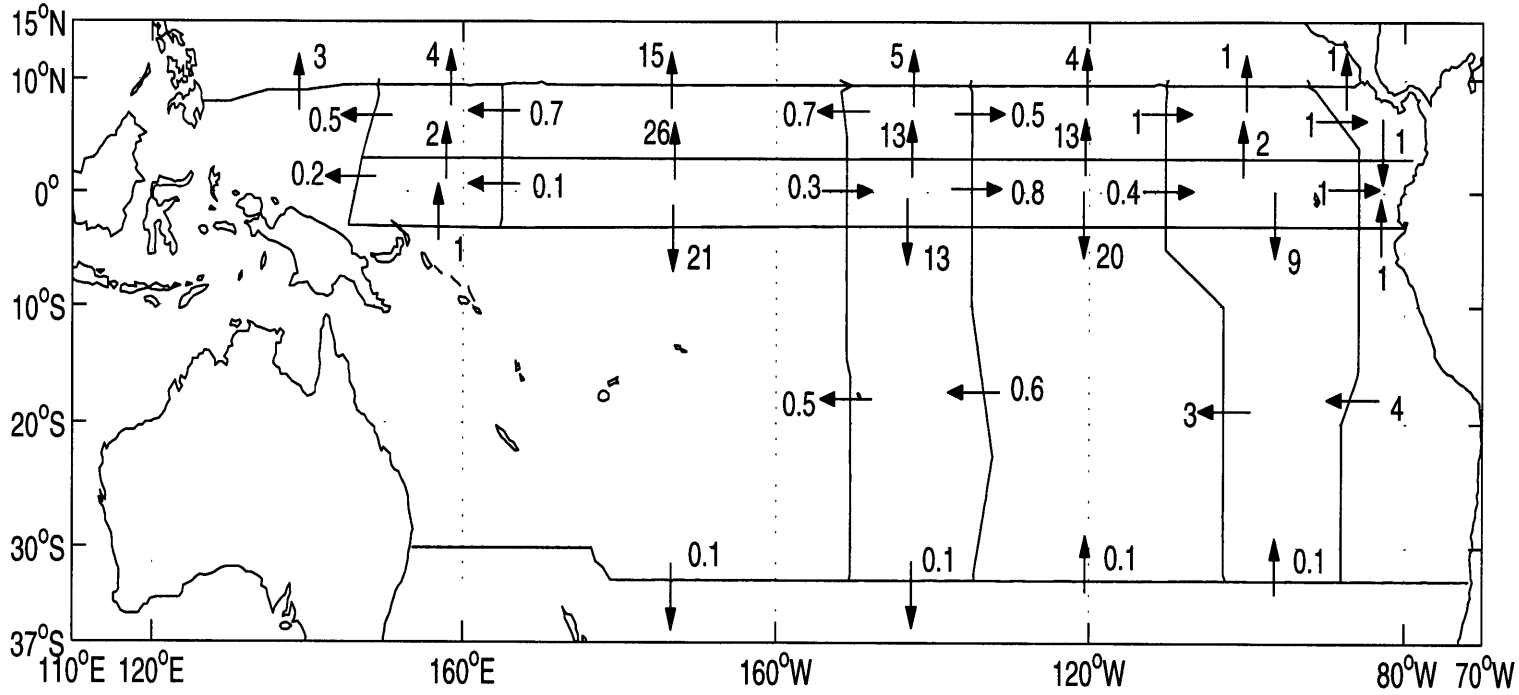

Figure 2-10: Ekman transport in Sv in the surface layer.

regions. There is a strong meridional divergence in the equatorial zone which is reduced or reversed when the geostrophic flow is also included. The zonal Ekman transport is also 1–2 orders of magnitude smaller than the meridional transport close to the equator as would be expected since the winds are mostly zonal.

Intermediate

The transports of intermediate waters are shown in Figure 2-11. Some of the transports, particularly across P41 and P42, appear to be rather large. However, it should be remembered that along these two sections the specified variance in the reference level velocities of 1 cms^{-1} is equivalent to a variance in the transport of intermediate water across a station pair of up to 100 Sv since the stations are very widely spaced. It is difficult to discern any large-scale pattern of the flow in this layer. *Wijffels* [1993] found that the flow in intermediate layers is dominated by large geostrophic eddies making it difficult to identify features of the mean flow despite using time-mean hydrographic data.

Deep

The deep water circulation is shown in Figure 2-12. Again, it is difficult to discern any large-scale features of the flow and in particular, the expected deep western boundary current is not apparent in this representation. Figure 2-13 shows the cumulative transports from east to west across sections P4 and P6. These plots show a generally northward transport across the western end and a generally southward transport across the eastern end of the two sections which is consistent with conventional ideas of deep water circulation in this basin.

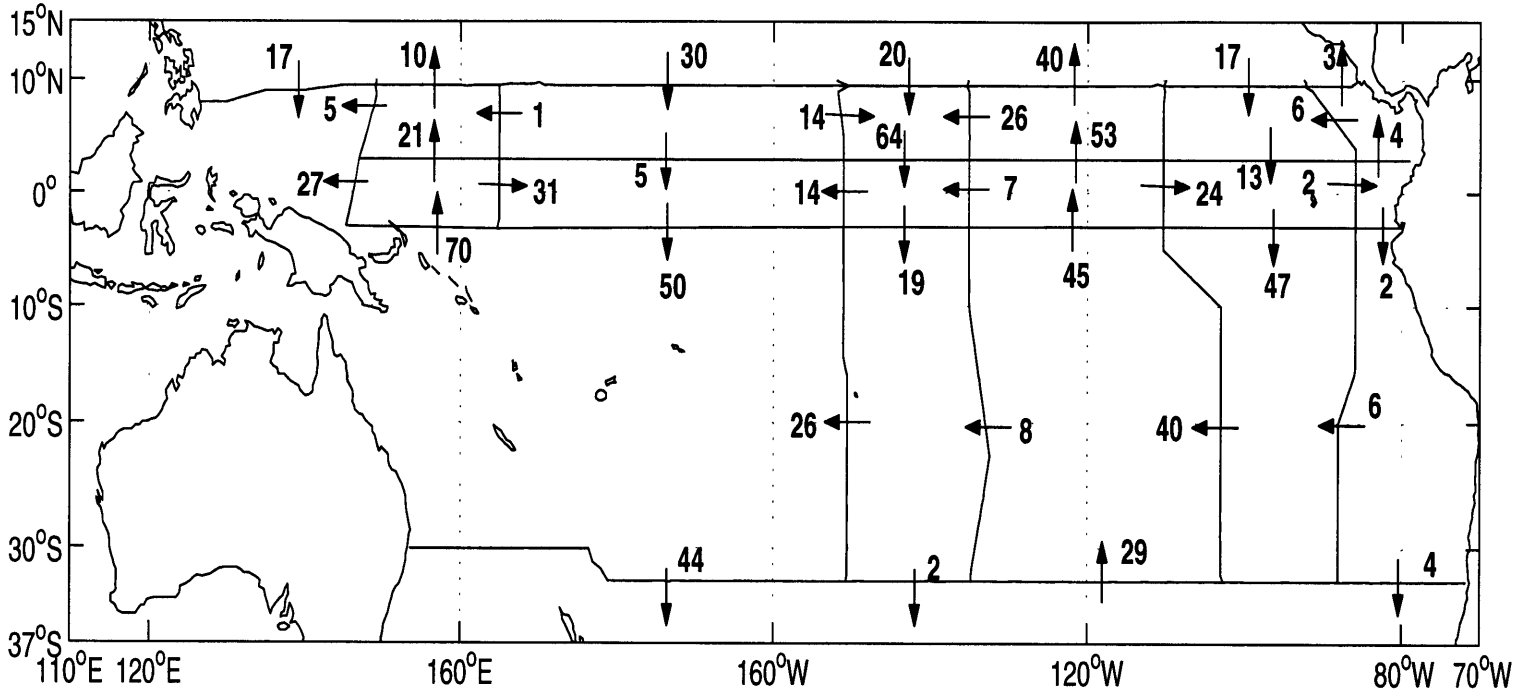

Figure 2-11: Transport in Sv in the intermediate layer. The numbers are the approximate magnitude of the transport in the direction of the arrows. Upwelling is not shown but that from the top of the layer would be the same as shown in Figure 2-8 and that through the base of the layer the same as that shown in Figure 2-12

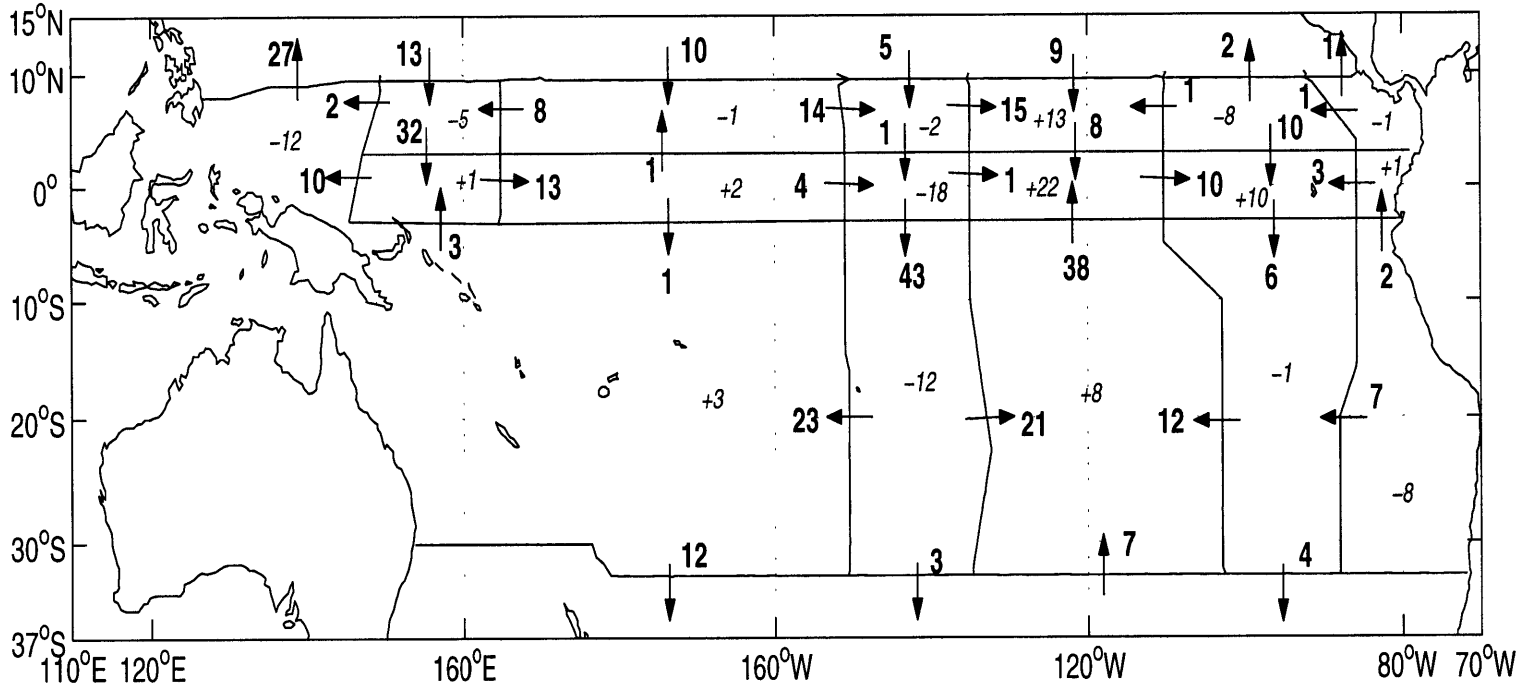

Figure 2-12: Transport in Sv in the deep layer. Bold numbers are the magnitude of the transport in the direction of the arrow. Smaller, italic numbers are the approximate magnitude of the upwelling through the top of the layer. Positive numbers are upwards, *out* of the layer.

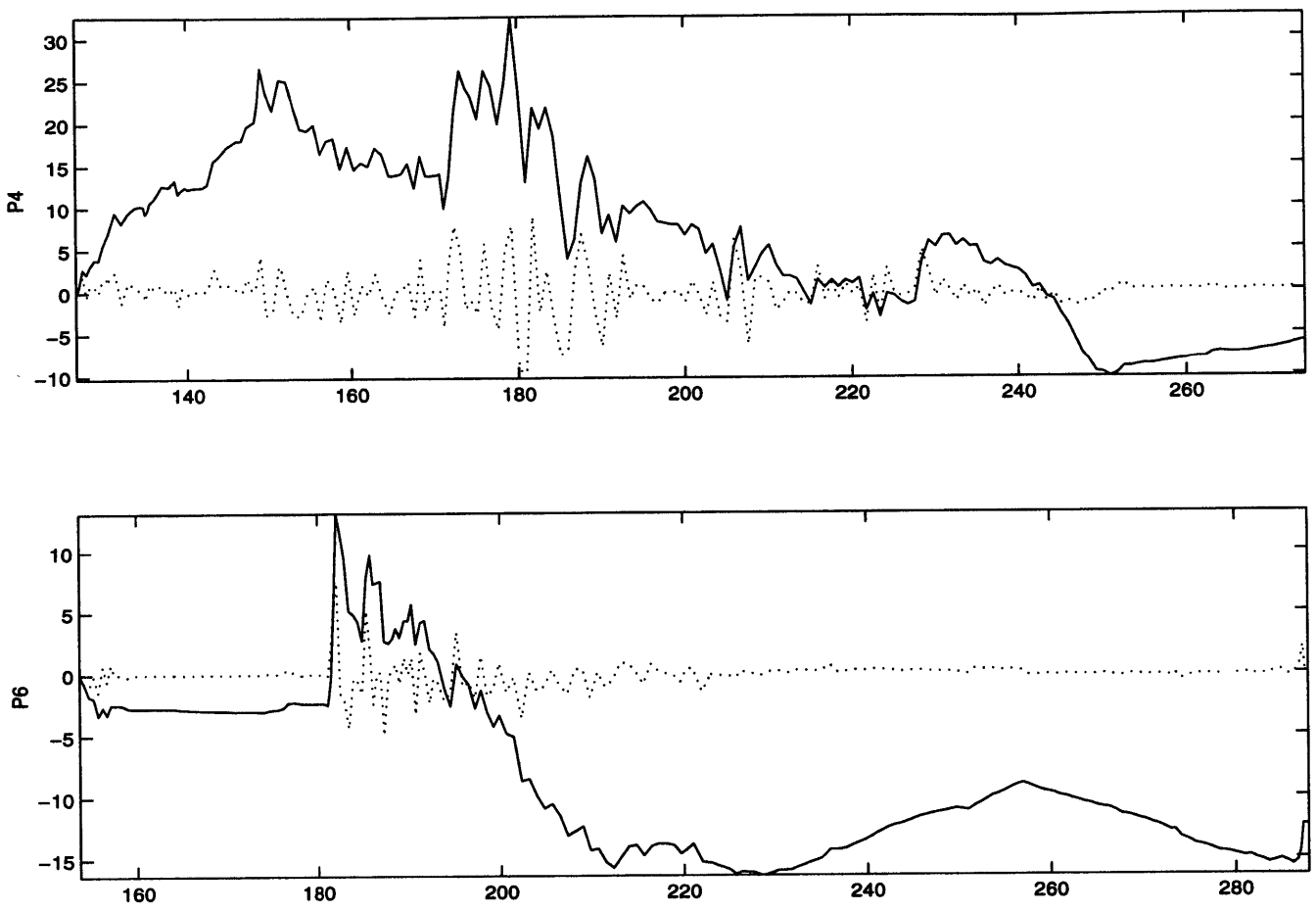

Figure 2-13: Transports across sections P4 (upper panel) and P6 (lower panel) in the deep layer in *Sv*. The solid line is the cumulative transport summed from east to west and the dotted line is the transport between each station pair

Isopycnal	Cross-isopycnal transport in Sv	Transport uncertainty in Sv
$\sigma_\theta = 23.5$	55	27
$\sigma_\theta = 24.5$	26	24
$\sigma_\theta = 25.5$	16	23
$\sigma_\theta = 26.2$	8	21
$\sigma_\theta = 26.7$	-6	20
$\sigma_\theta = 27.1$	0	18
$\sigma_2 = 36.5$	6	18
$\sigma_2 = 36.75$	8	17
$\sigma_2 = 36.85$	14	17
$\sigma_2 = 36.95$	19	16
$\sigma_4 = 45.81$	9	15
$\sigma_4 = 45.85$	-4	13

Table 2.3: Cross-isopycnal transport in steady state model

2.3.4 Vertical transports

In general, there is strong upwelling in the upper layers of the equatorial boxes and downwelling in the upper layers of the northern and southern boxes. The total cross-isopycnal transports for the equatorial zone is shown in Table 2.3. The upwelling is strongest across the $\sigma_\theta = 23.5$ isopycnal. This is not surprising since the upwelling is dominantly required to balance the Ekman divergence from the equatorial boxes and in this model the Ekman transport is assumed to be entirely in the surface layer. It is difficult to make a comparison of these estimates with those mentioned in section 1.1 since a different area is covered but this estimate is of an order of magnitude consistent with previous estimates.

Table 2.4 shows the mean cross-isopycnal velocity across each isopycnal in the equatorial zone. The mean vertical velocities are at the low end of the range of estimates given in section 1.1 but are a reasonable magnitude. It should be remembered that these are not strictly vertical velocity but the velocity perpendicular to the isopy-

Isopycnal	Cross-isopycnal velocity ($10^{-4}cms^{-1}$)	Uncertainty ($10^{-4}cms^{-1}$)
$\sigma_\theta = 23.5$	6.88	3.23
$\sigma_\theta = 24.5$	4.54	3.04
$\sigma_\theta = 25.5$	3.93	2.91
$\sigma_\theta = 26.2$	3.10	2.70
$\sigma_\theta = 26.7$	-1.11	2.45
$\sigma_\theta = 27.1$	0.02	2.10
$\sigma_2 = 36.5$	-0.86	2.03
$\sigma_2 = 36.75$	0.48	2.00
$\sigma_2 = 36.85$	0.46	1.98
$\sigma_2 = 36.95$	1.97	2.39
$\sigma_4 = 45.81$	-0.28	2.27
$\sigma_4 = 45.85$	-2.06	2.03

Table 2.4: Cross-isopycnal transport in steady state model

cnal surface so it is perhaps not surprising that these estimates are at the smaller end of the expected range.

Although the zonal mean vertical transport and velocity is upwards, there is significant downwelling in areas 8 and 11 (Figure 2-7i). This is unexpected, *Philander et al.* [1987] in a modelling study found upwelling at all meridions, and it is not clear whether the downwelling at the base of the thermocline seen here is a real feature of the the steady circulation or related to some problem with the input data. The downwelling in area 8 may be a real feature - water may be upwelled from the EUC in the east Pacific, recirculated through surface currents and downwelled back into the EUC in the western Pacific. The sense of the transports shown in Figure 2-8 suggest that such a pathway is feasible to the south of the equator, through the SEC, since there is generally southward transport across the eastern end of P42 and northward transport into area 8 across P42. It would seem more likely that the downwelling in area 11 is the result of inadequate data - there are large residuals of the same sense in the top five model layers so that over the whole thermocline there is a strong

Reference level velocities		$\pm 1 cms^{-1}$
Vertical velocities		$\pm 5 \times 10^{-4} cms^{-1}$
except	upper 5 layers in equatorial zone	$\pm 5 \times 10^{-3} cms^{-1}$
box imbalances (boxes 1–18)		$\pm 5 Sv$
except	boxes in contact with surface	$\pm 10 Sv$
box imbalances (boxes 19–24)		$\pm 2 Sv$
except	boxes in contact with surface	$\pm 3 Sv$

Table 2.5: Summary of the constraints applied to the model

divergence in this area.

2.4 Summary

An inverse box model has been setup, incorporating mass, salt and heat conservation statements and solved using the constraints shown in Table 2.4.

The circulation pattern found is in good agreement with previous descriptions of the circulation of the region and the estimates of the zonal mean vertical transport of 55 ± 27 Sv and vertical velocity of $6.88 \pm 3.23 \times 10^{-4}$ cms^{-1} are also of the same order of magnitude of prior estimates.

Chapter 3

Time Dependent Model

3.1 Model Equations for $\Delta^{14}C$

Bomb radiocarbon is a transient tracer and so the time dependent version of the general advective tracer equation must be used (equation 3.1).

$$\frac{\partial C}{\partial t} + \mathbf{v}.\nabla C = Q(\mathbf{x}, t) \tag{3.1}$$

Following the method of *Wunsch* [1984], this equation may be integrated over volume and time to give equation 3.2.

$$\begin{aligned}\sum_j \rho_j b_j \Delta a_j \int_{t_1}^{t_2} \Delta^{14}C_j \, dt + w_B A \int_{t_1}^{t_2} \overline{\Delta^{14}C_B}(t) \, dt - w_T A \int_{t_1}^{t_2} \overline{\Delta^{14}C_T}(t) \, dt \\ = -\sum_j \rho_j v_j \Delta a_j \int_{t_1}^{t_2} \Delta^{14}C_j(t) \, dt - \sum_j F_{ek} \int_{t_1}^{t_2} \Delta^{14}C_j(t) \, dt \\ - \left[\overline{\Delta^{14}C}(t_2) - \overline{\Delta^{14}C}(t_1)\right] V - \frac{1.1EA}{\Sigma CO_2} \int_{t_1}^{t_2} [\Delta^{14}C_{atm}(t) - \Delta_{14}C_{surf}(t)] \, dt\end{aligned} \tag{3.2}$$

The LHS and the first two terms on the RHS are the same as those appearing in the steady state equation (Equation 2.4). The additional two terms are the change in

the radiocarbon inventory of the box and an atmospheric source term where E is the invasion rate and ΣCO_2 is the total carbon.

3.1.1 Time history of $\Delta^{14}C_{atm}$

The atmospheric $\Delta^{14}C$ is based on Figure 17 of *Broecker et al.* [1995]. The curve for the global mean tropospheric $\Delta^{14}C$ is used here since the model domain spans the northern and southern hemispheres. The rise in concentration from 0‰ in 1955 to a peak value of 725‰ in 1965 was represented by a quadratic function which was judged to give a better representation than either linear or exponential rises. The decay from the peak value to about 125‰ in 1992 was modelled as an exponential function. This was written as

$$\Delta^{14}C_{atm}(t) = 7.25(t - 1955)^2 \qquad 1955 \leq t \leq 1965 \tag{3.3}$$

$$\Delta^{14}C_{atm}(t) = 725e^{(1965-t)/\tau} \qquad 1965 \leq t \leq 1992 \tag{3.4}$$

$$\tau = 14.2yrs$$

3.1.2 Invasion rate

Wunsch [1984] used a value of $E = 16 \pm 4molm^{-2}yr^{-1}$ based on a survey of prior estimates. *Quay et al.* [1983] estimated $E = 15 \pm 3molm^{-2}yr^{-1}$ as giving the best model fit to observations and *Broecker et al.* [1985] estimated $E = 19.4molm^{-2}yr^{-1}$ for the Pacific Ocean by requiring that the change in ocean bomb-^{14}C inventory is equal to the bomb-^{14}C input to the ocean but gave no estimate of the possible error. The estimate of *Wunsch* [1984] is adopted here.

3.1.3 Time history of $\Delta^{14}C_{surf}$

There is no significant change in surface bomb $\Delta^{14}C$ between the GEOSECS survey and WOCE [*Peng et al.*, 1998] and so again the method of *Wunsch* [1984] is adopted here to describe $\Delta^{14}C_{surf}$. It is assumed that $\Delta^{14}C_{surf}$ rises linearly from its pre-bomb value to its post-bomb value between 1959 and 1968 (as given in equation 3.5) and remains constant from 1968 to 1992.

$$\Delta^{14}C_{surf}(t) = \Delta^{14}C_{surf,pre} + \frac{(1968 - t)}{(1968 - 1959)}(\Delta^{14}C_{surf,post} - \Delta^{14}C_{surf,pre}) \qquad (3.5)$$

3.1.4 Total Carbon

Only a small error is introduced by assuming that ΣCO_2 is constant over the whole region. *Wunsch* [1984] used a value of 2.1 molm^{-3} and *Broecker et al.* [1985] used ΣCO_2 = 2.15 molm^{-3}. A more recent estimate study of *Jain et al.* [1995] used a model estimated value of 2.1 molm^{-3}. These estimates are all in good agreement and here $\Sigma CO_2 = 2.1 molm^{-3}$ is used.

3.1.5 Time history of subsurface $\Delta^{14}C$

The subsurface $\Delta^{14}C$ was assumed to rise linearly from its pre-bomb value to its present value over a nine year period. The time at which the values start to rise is taken to be a linear function of depth, ranging from 1959 at the surface to 1992 at 600m, the calculated mean penetration depth. In the upper 600m, the pre-bomb $\Delta^{14}C$ values were calculated using the correlation with silicate described by *Broecker et al.* [1995]. The mean penetration depth was calculated by finding the depth at which the reconstructed pre-bomb $\Delta^{14}C$ profile intersected the observed $\Delta^{14}C$ profile in each station pair and then taking a mean value over all station pairs.

3.1.6 Errors in $\Delta^{14}C$ terms

Errors in the radiocarbon budget arise from uncertainty in the mass budget, the atmospheric source term and the volume storage term. The mass imbalance is kept the same as in the previous model. The source terms and volume storage terms are both assumed to have an error of 25%.

3.2 Model results

A solution was found with the same constraints as described in the previous chapter. In this case, 83% of model residuals, 96% of reference level velocities and 85% of cross-isopycnal velocities were within the specified constraints. This is not quite as high as that achieved in the previous model, as would be expected since another set of constraints (the ^{14}C data) has been added. However, the solution is still considered to be acceptable and the details of the solution are shown in Figures 3-1a – 3-1i. These are the same as Figures 2-6a–2-6i except the model includes the radiocarbon data and the modified constraints are used. The solution is very similar to that described in the previous chapter. It appears that the uncertainty in the model residuals, particularly in the upper layers, is increased. It would be expected that the inclusion of the radiocarbon constraints would have the most impact in the upper layers since it is assumed that there has been no change in the radiocarbon distribution in the deeper layers and so no new information is included for these layers. The most significant difference can be seen in the vertical velocity profiles.

3.2.1 Horizontal circulation

The circulation in the thermocline, intermediate and deep layers (as defined in the previous chapter) are shown in Figure 3-2a, 3-2b and 3-2c and the cumulative trans-

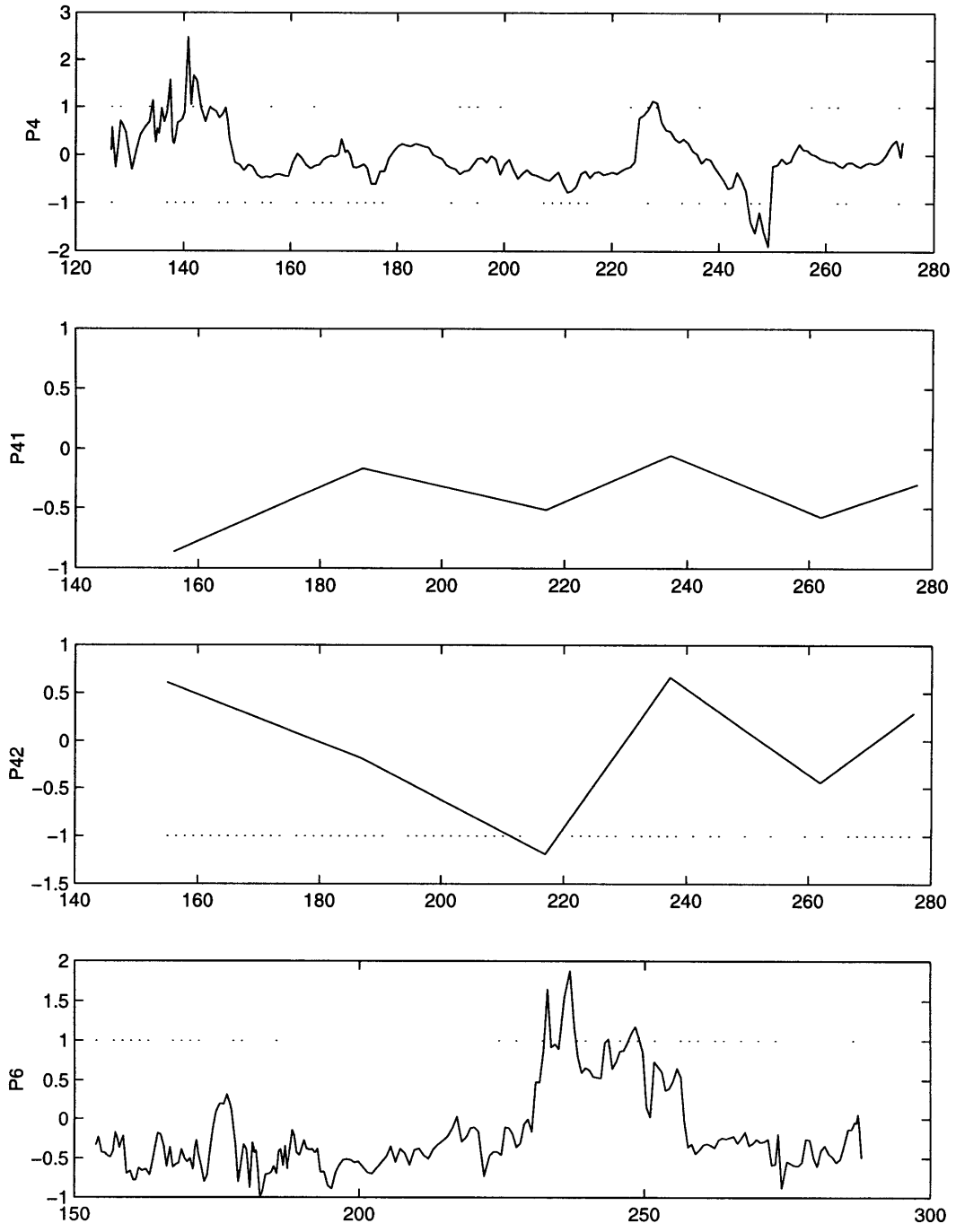

Figure 3-1a: Reference level velocities along zonal sections

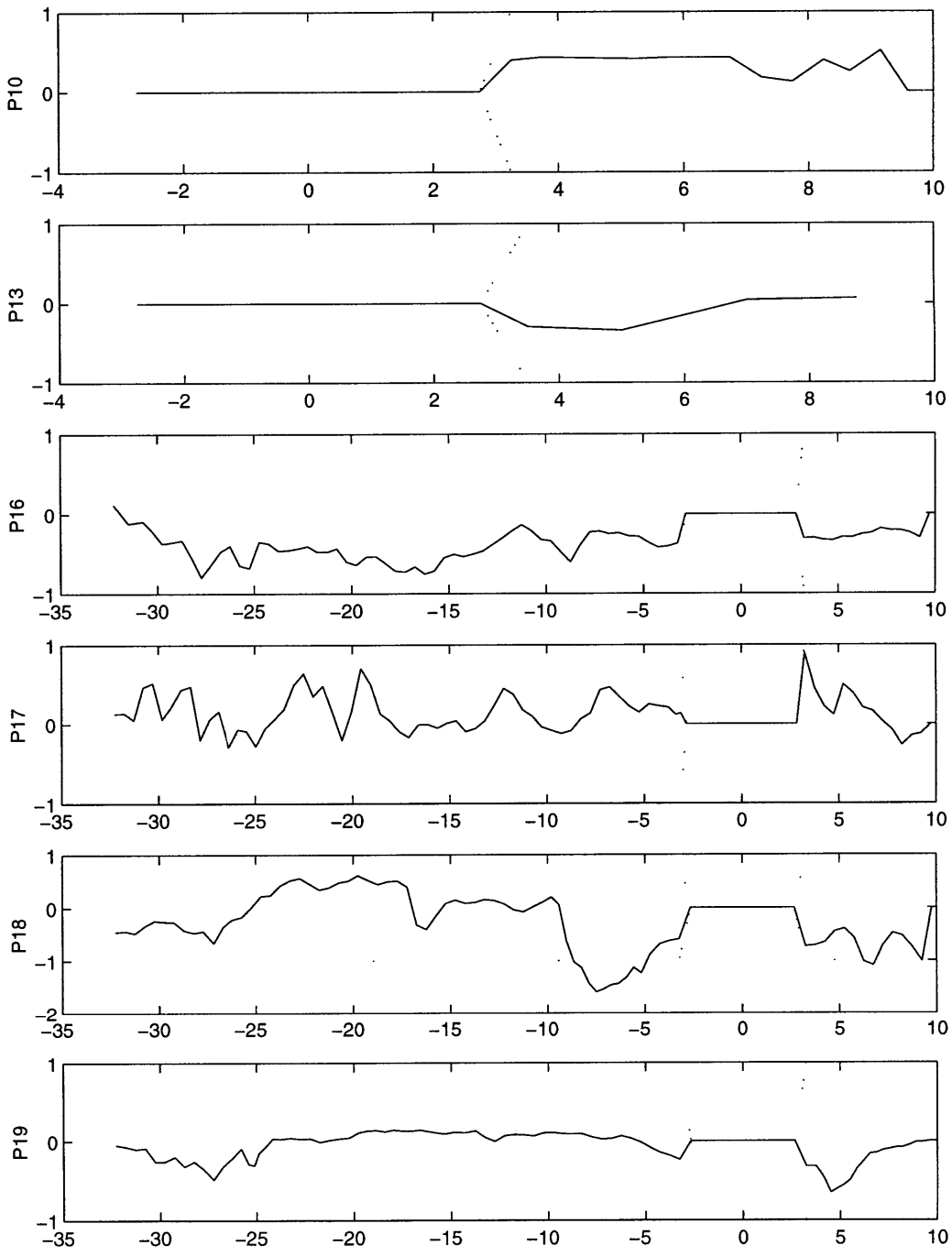

Figure 3-1b: Reference level velocities along meridional sections

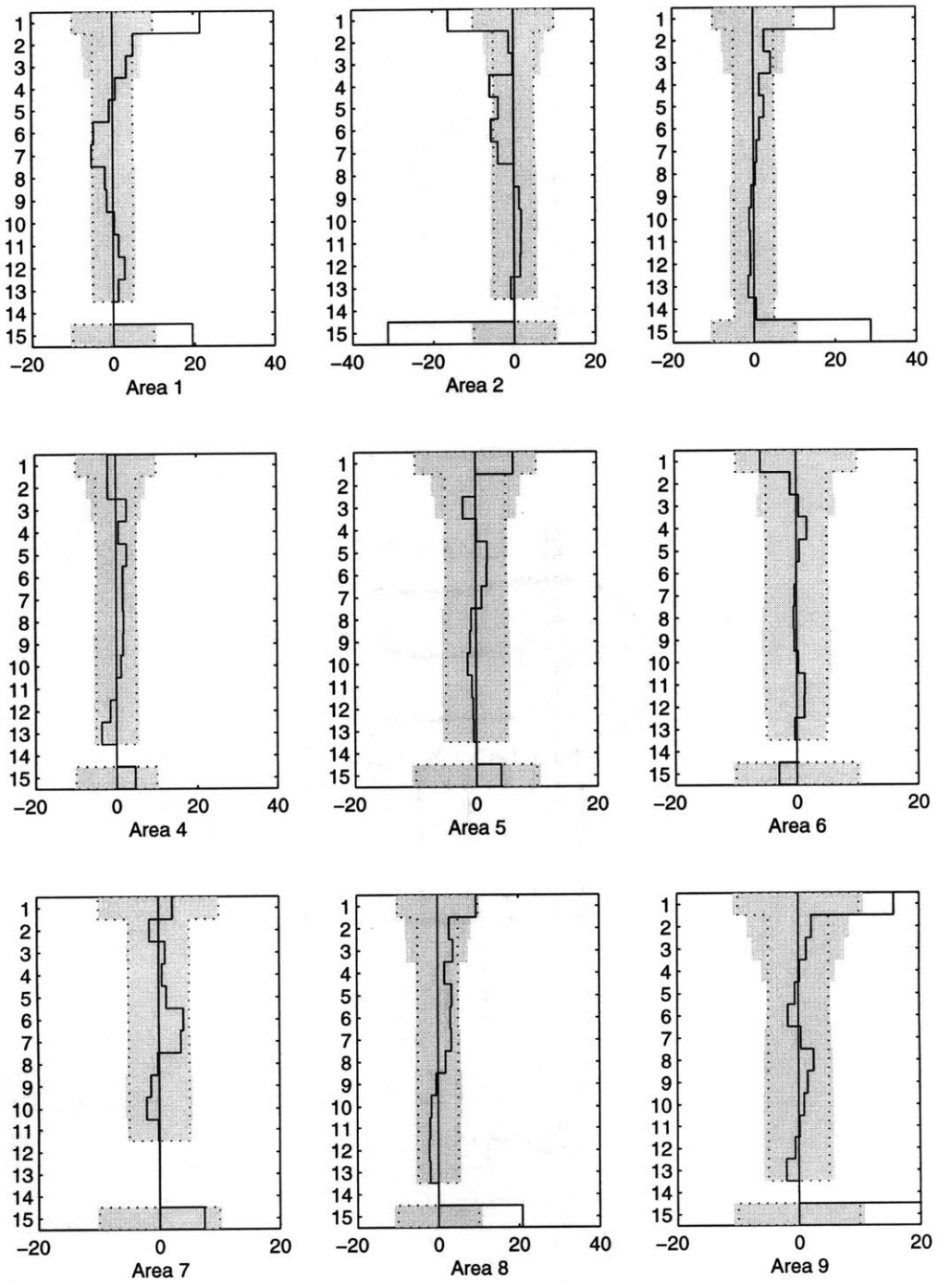

Figure 3-1c: Model residuals in areas 1–9

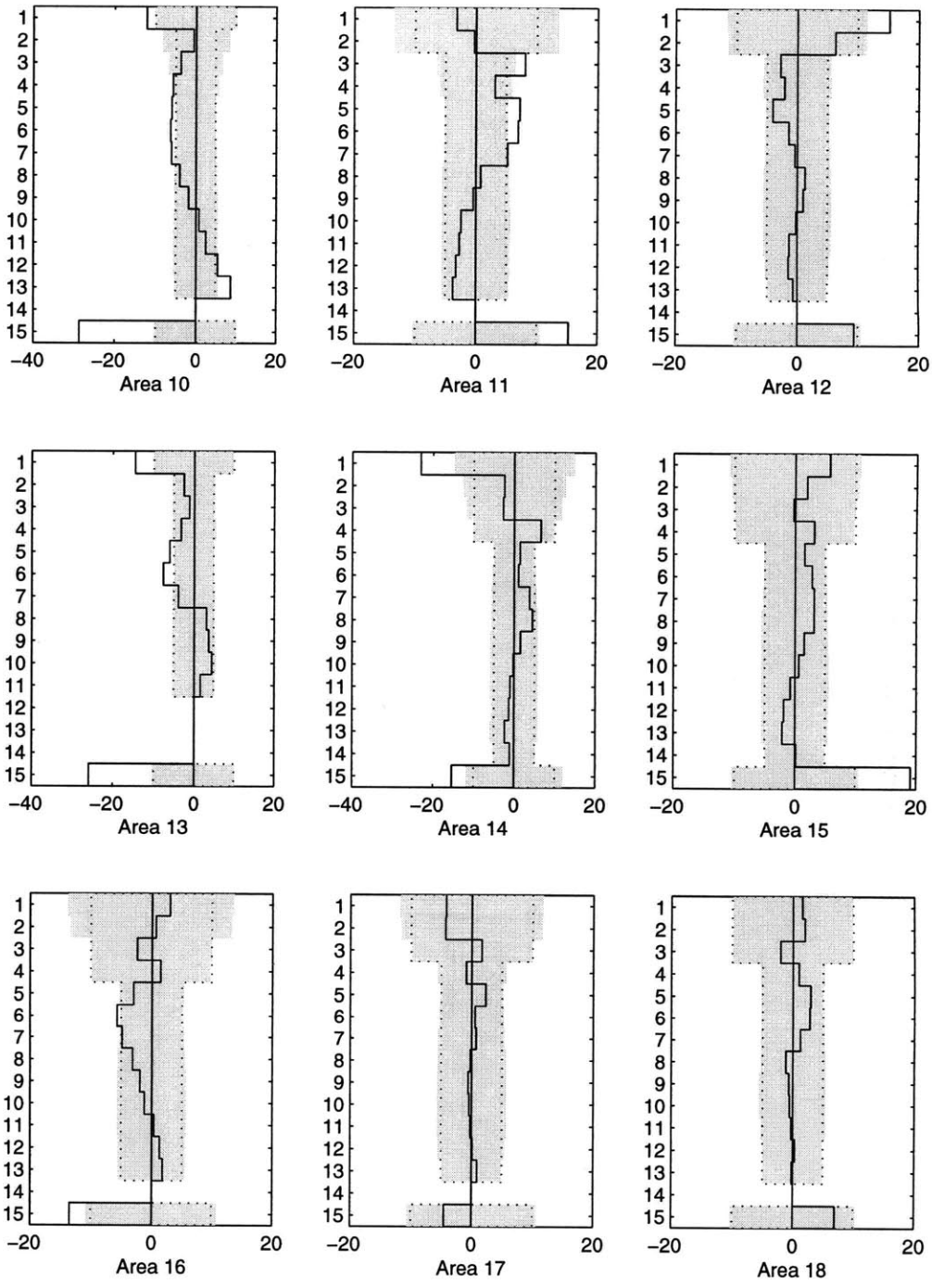

Figure 3-1d: Model residuals in areas 10-18

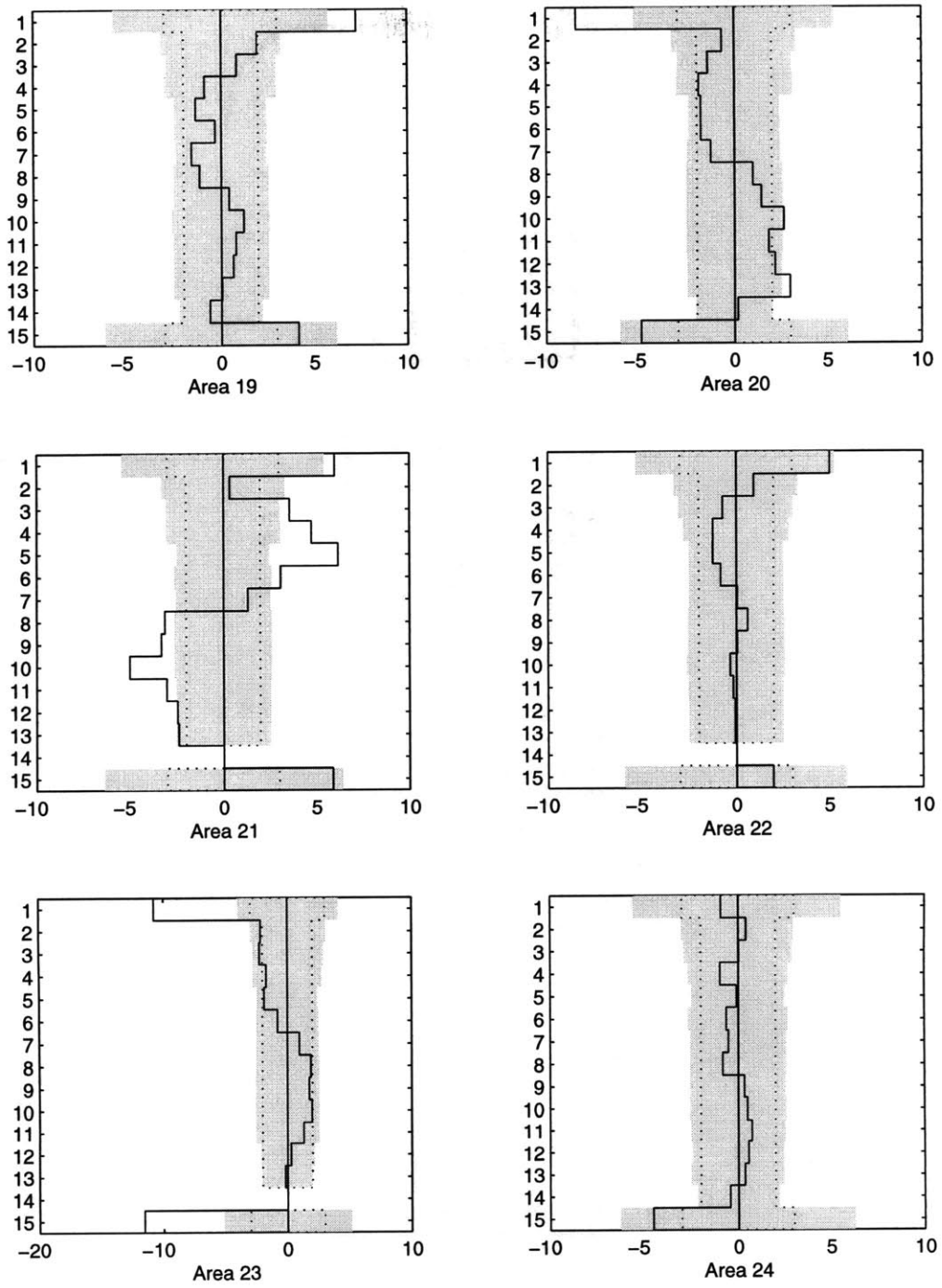

Figure 3-1e: Model residuals in areas 19-24

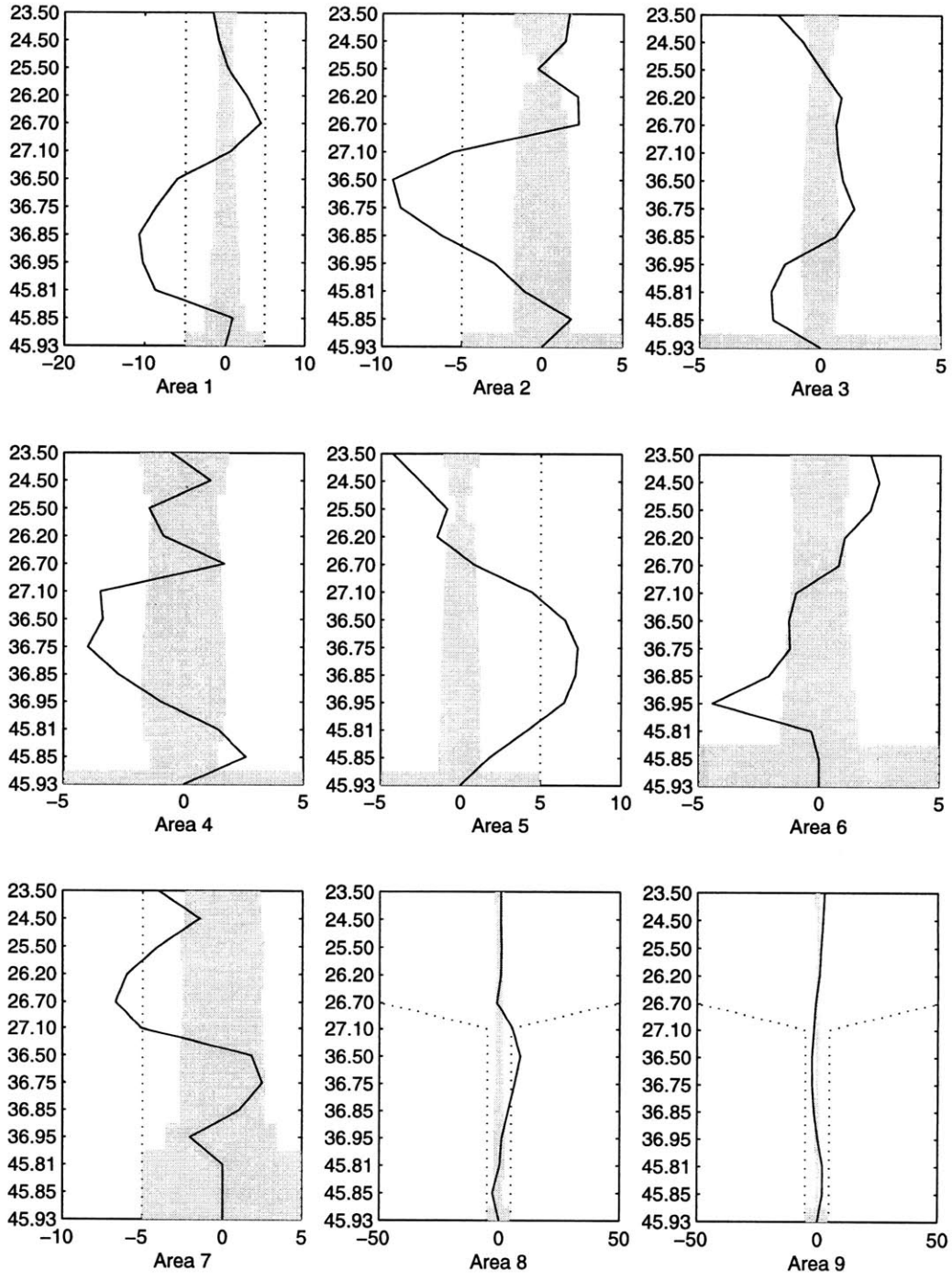

Figure 3-1f: Vertical velocities in areas 1–9

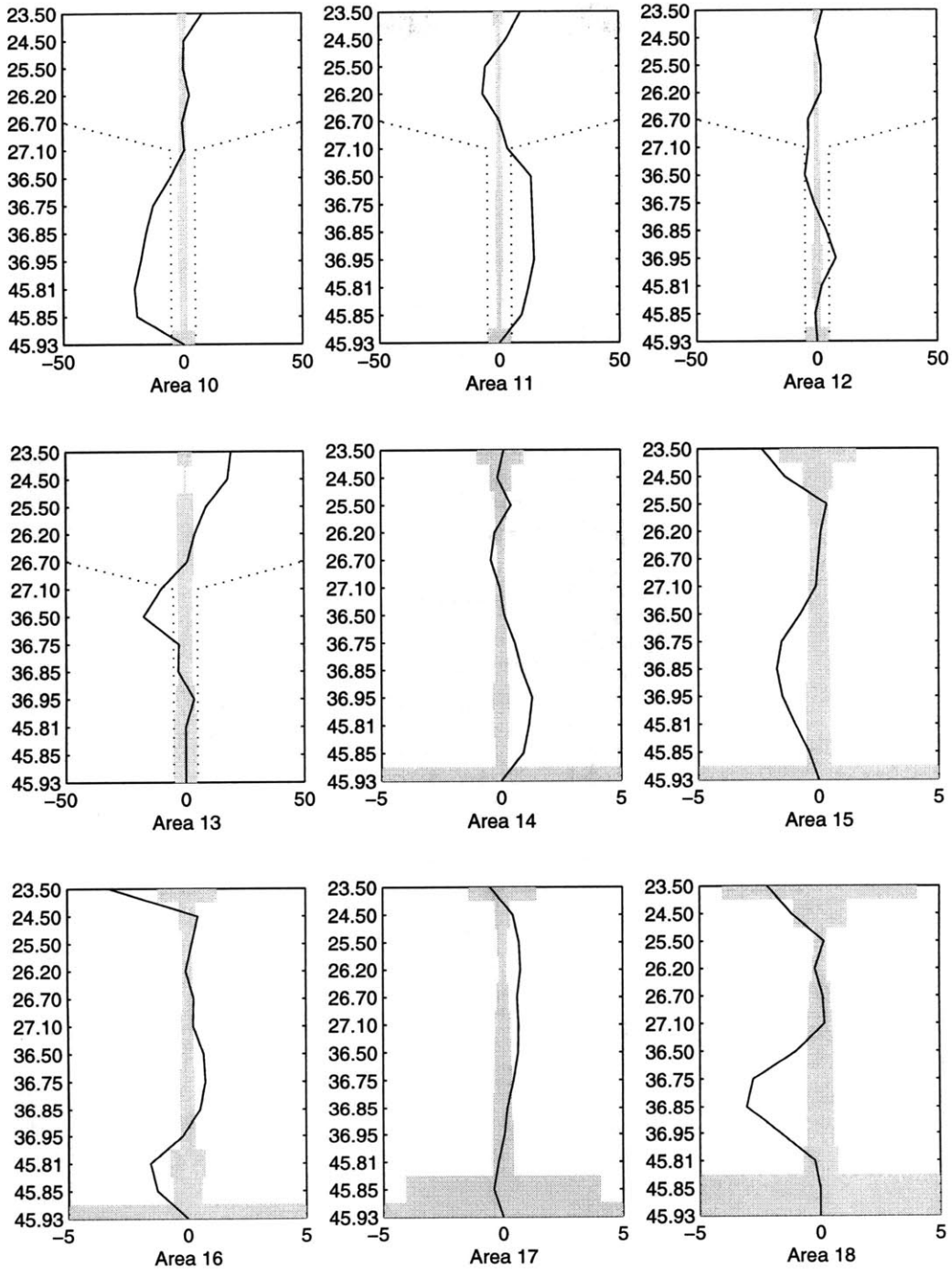

Figure 3-1g: Vertical velocities in areas 10-18

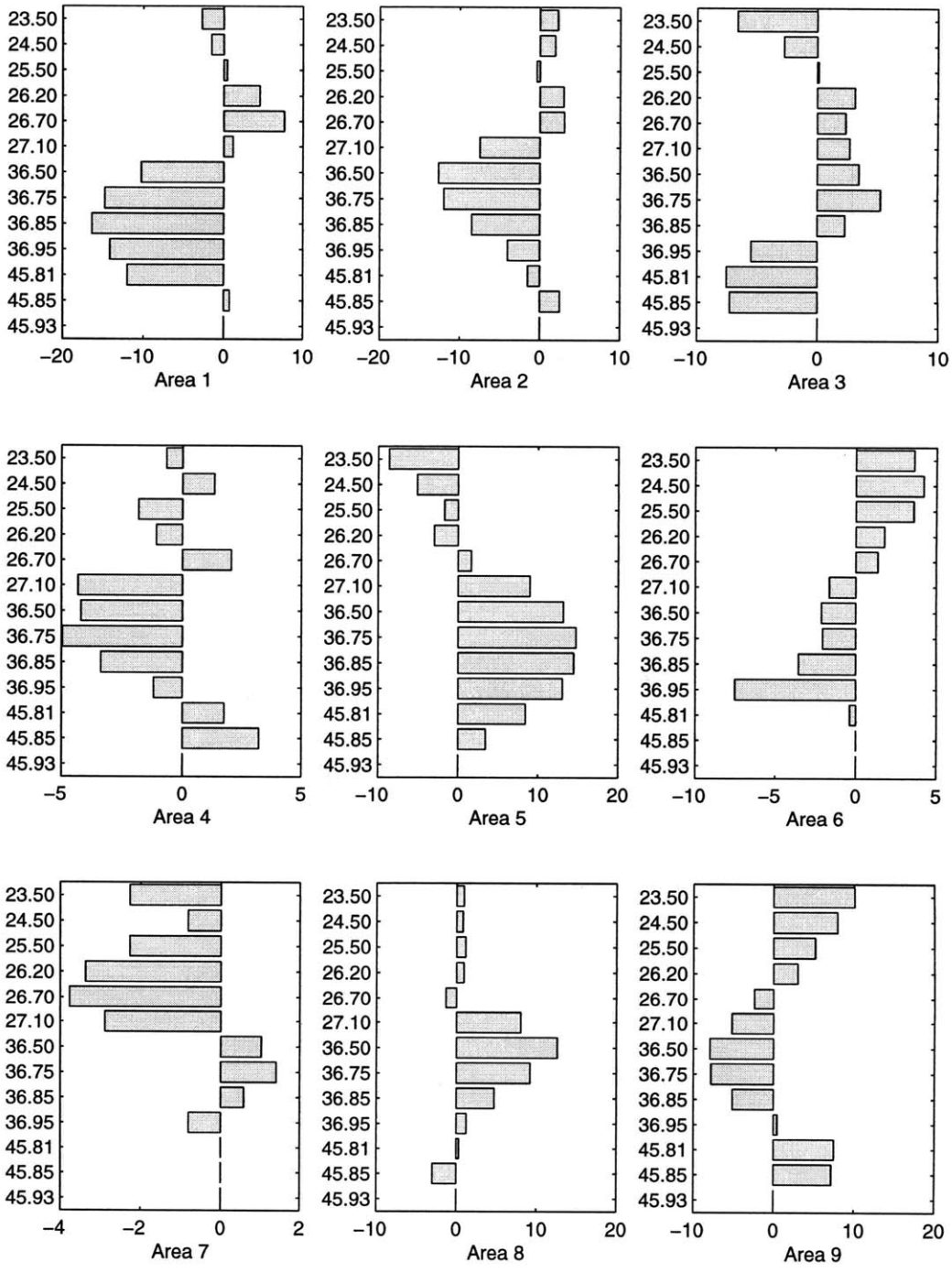

Figure 3-1h: Cross-isopycnal transports in areas 1–9

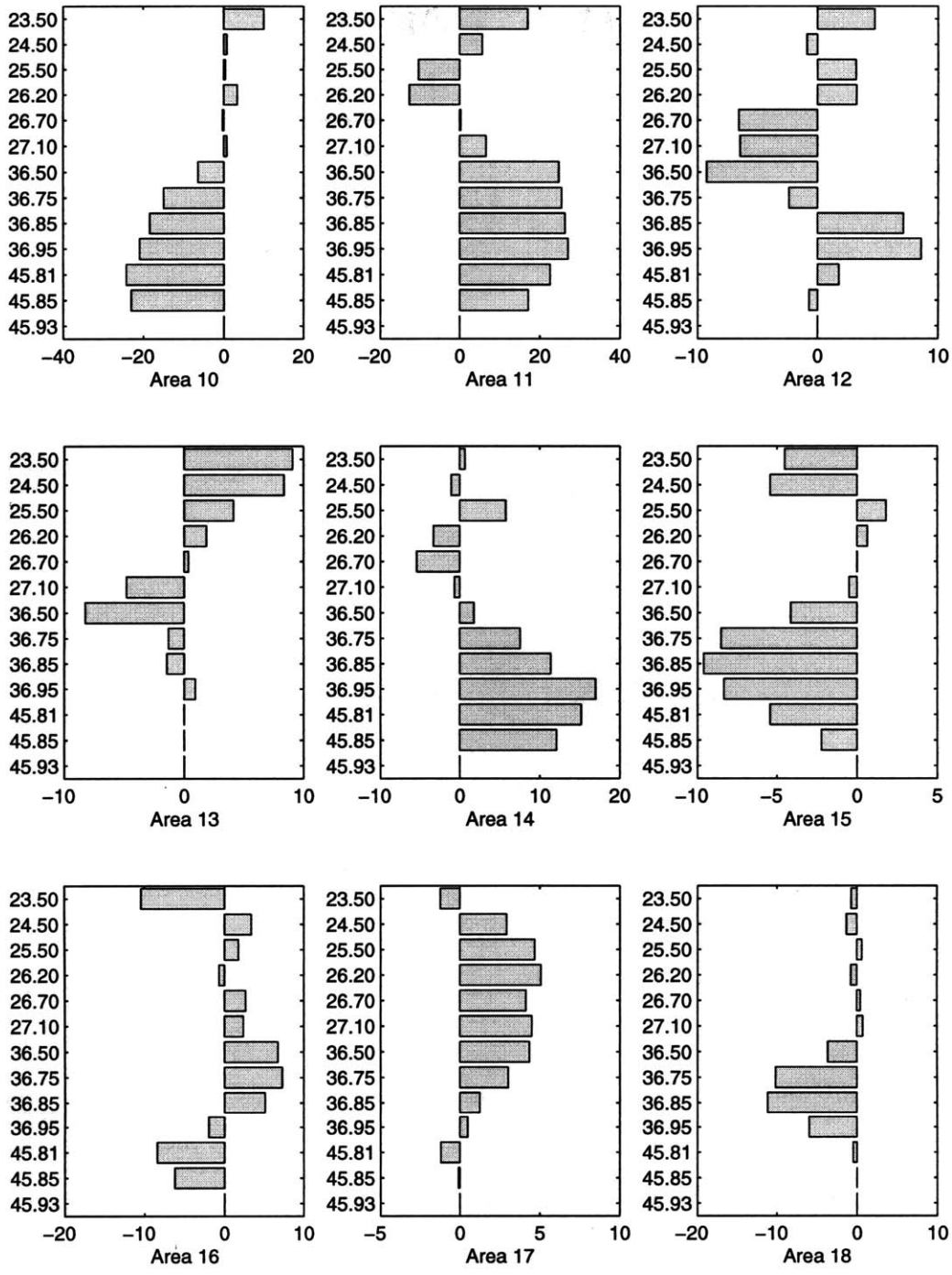

Figure 3-1i: Cross-isopycnal transports in areas 10–18

Isopycnal	Cross-isopycnal transport in Sv	Transport uncertainty in Sv
$\sigma_\theta = 23.5$	52	16
$\sigma_\theta = 24.5$	23	8
$\sigma_\theta = 25.5$	4	12
$\sigma_\theta = 26.2$	0	11
$\sigma_\theta = 26.7$	-10	11
$\sigma_\theta = 27.1$	-1	12
$\sigma_2 = 36.5$	5	13
$\sigma_2 = 36.75$	8	13
$\sigma_2 = 36.85$	13	13
$\sigma_2 = 36.95$	17	14
$\sigma_4 = 45.81$	8	11
$\sigma_4 = 45.85$	-2	9

Table 3.1: Cross-isopycnal transport in time dependent model

ports across P4 and P6 in the deep layer in Figure 3-2d. These are very similar to the circulation pattern found in the steady-state version of the model. These have been described in the previous chapter and are not discussed again here.

3.2.2 Vertical Transports

The total cross-isopycnal transport for the equatorial zone is shown in Table 3.1.

The magnitude of the upwelling is very similar to that found in the steady state model but the uncertainties are significantly reduced. This is to be expected because radiocarbon is a strong constraint on vertical transfer since the observed distribution is mostly the result of a balance between the downward diffusion of bomb-radiocarbon and the upwelling of bomb-^{14}C free waters.

Table 3.2 shows the zonal mean cross-isopycnal velocity in the equatorial region. Again, compared with the results from the previous model, the uncertainties are strongly reduced, particularly in the upper layers. The upwelling across the isopycnals

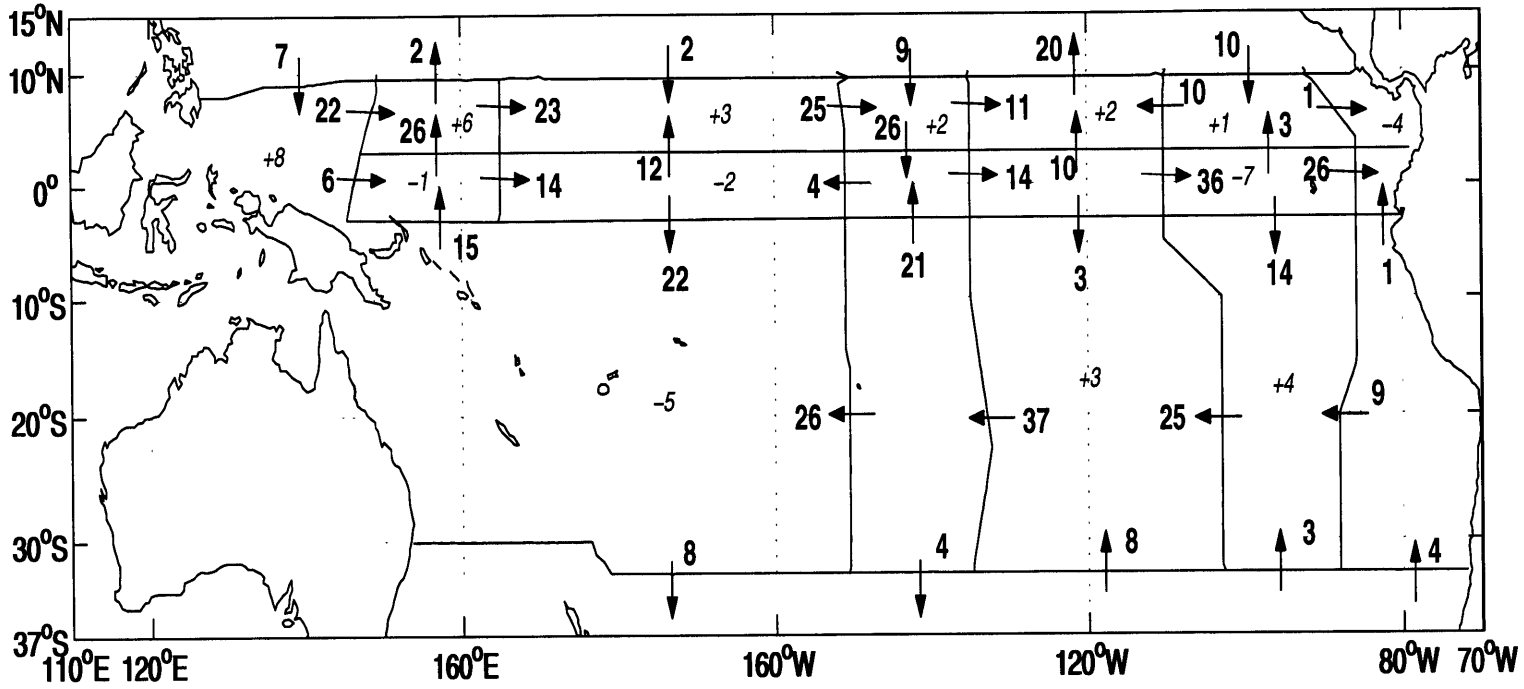

Figure 3-2a: Transport in the thermocline layer, as for Figure 2-8 but for model including ^{14}C.

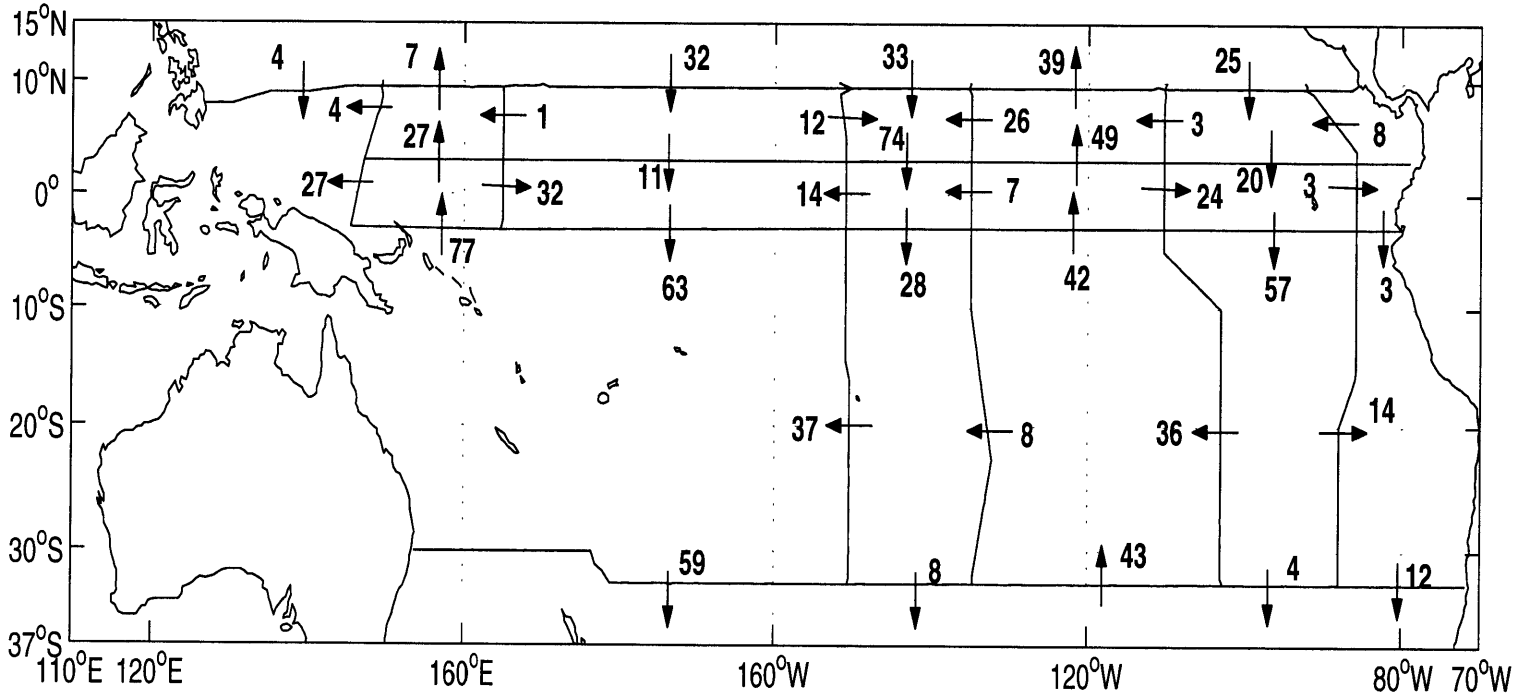

Figure 3-2b: Transport in the intermediate layer as for Figure 2-11 except that transports through the top of the layer are the same as those shown in Figure 3-2a and those through the bottom of the layer as in Figure 3-2c.

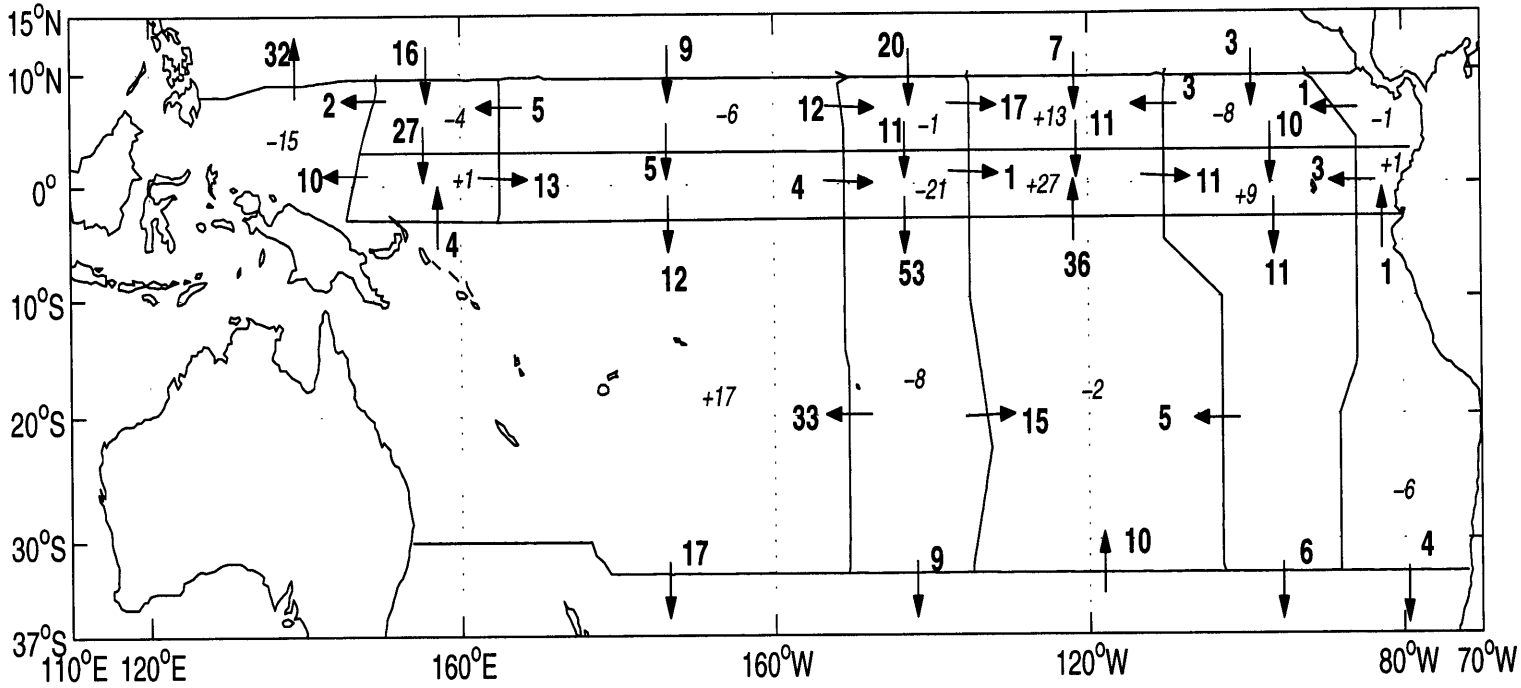

Figure 3-2c: Transport in the deep layer as for Figure 2-12 but for model with ^{14}C constraints.

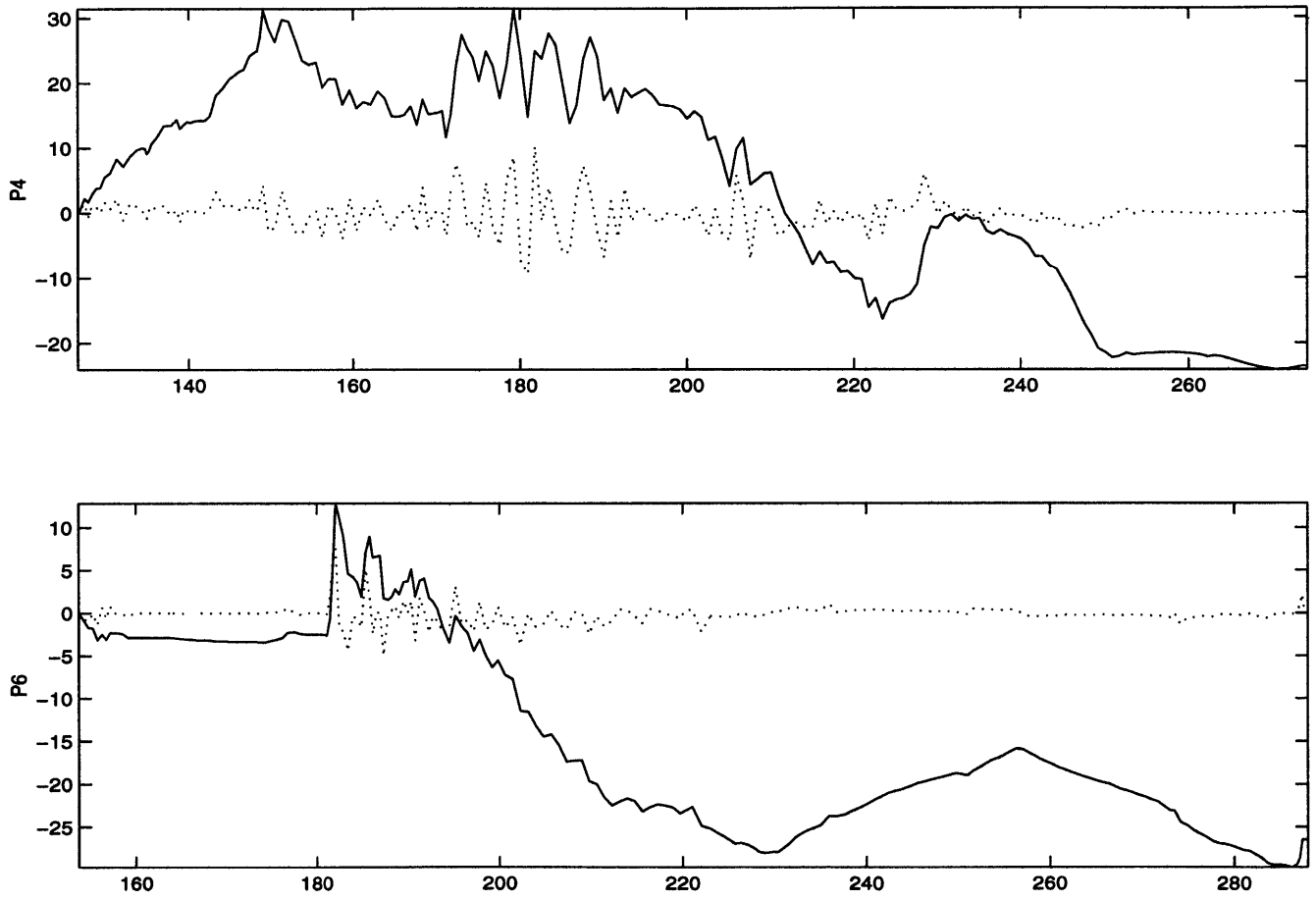

Figure 3-2d: Cumulative transport in the deep layer as for Figure 2-13 except for model including ^{14}C constraints.

Isopycnal	Cross-isopycnal velocities ($10^{-4}cms^{-1}$)	Uncertainty ($10^{-4}cms^{-1}$)
$\sigma_\theta = 23.5$	7.15	1.90
$\sigma_\theta = 24.5$	3.97	0.80
$\sigma_\theta = 25.5$	1.25	1.51
$\sigma_\theta = 26.2$	0.53	1.42
$\sigma_\theta = 26.7$	-0.74	1.50
$\sigma_\theta = 27.1$	-0.89	1.53
$\sigma_2 = 36.5$	-1.34	1.56
$\sigma_2 = 36.75$	0.22	1.61
$\sigma_2 = 36.85$	0.30	1.66
$\sigma_2 = 36.95$	1.59	2.11
$\sigma_4 = 45.81$	-0.64	2.16
$\sigma_4 = 45.85$	-1.91	1.86

Table 3.2: Cross-isopycnal transport in time dependent model

$\sigma_\theta = 25.5$ and $\sigma_\theta = 26.2$ is much less than in the previous model suggesting that most of the water that upwells into the mixed layer comes from the middle of the thermocline rather than the base of the thermocline.

3.3 Summary

The model described in the previous chapter has been modified to include radiocarbon constraints. The horizontal circulation pattern is very similar to that previously found, but the radiocarbon has provided a strong constraint on the vertical transfers in the surface layers and has significantly reduced the estimated error. The maximum total upwelling in the equatorial zone is now estimated to be $52 \pm 16Sv$ and the maximum zonal mean cross-isopycnal velocity is estimated as $7.15 \pm 1.90 \times 10^{-4}cms^{-1}$

Chapter 4

Discussion

4.1 Summary of results

An inverse box model has been set up using the new WOCE hydrographic, LADCP and radiocarbon data. The maximum upwelling in the equatorial Pacific is found to be $52 \pm 16 Sv$. The inclusion of the radiocarbon data significantly reduced the error on the estimates of upwelling rate in the upper layers. However, the question still remains of how well the input one-time data represents the mean state of the ocean in a region of such high variability. *Firing et al.* [1998] note that individual sections from the Pacific Equatorial Ocean Dynamics (PEQUOD) program differed substantially from the mean and it would seem likely that the same is also true of the WOCE sections.

4.1.1 Model improvements

There are several improvements which could be made to this model which may help to improve the estimate of the equatorial upwelling. Flux constraints were not used and the addition of these may have a significant impact on the transports found. The

north Pacific Ocean is an almost closed basin, the flow through the Bering Straits is of order 1 Sv, therefore any mass flux out of the Pacific, that is the Pacific-Indian throughflow, must be balanced by a similar flux into the South Pacific. One would anticipate that the net mass flux across sections P6 and P42 was of the order of 15 Sv and that across P41 and P4 of only around 1 Sv. Greater independence of the box-balance equations could be achieved by using salt and temperature anomaly equations. The variations of salinity and temperature are only a small percentage of the total salt or heat content and so the conservation statements for these are almost the same as those for mass [*Wijffels*, 1993]. A more rigorous estimate of the expected variances could also be made. In this model, the specified statistics were based on the constraints used in previous work and were then modified somewhat arbitrarily to account for the large variability known to exist in this region. An examination of the sources of error, such as that of *Ganachaud* [1999] who proposes a variability of ± 20 Sv at a latitude of 5^o, may significantly change some of the constraints used here. The pre-processing of the radiocarbon data could be improved - the method of interpolation used here was the simplest possible. An improved interpolation method, for example using objective mapping, may give a more reliable estimate of the ^{14}C distribution, particularly along the sections where the data are sparse (P4, P41 and P42). Finally, in this version of the model, only one term for cross-isopycnal transfers was included and this was assumed to represent all the transport across a surface due to advection, diffusion and mixing. However, given that the radiocarbon distribution is a balance between two opposite processes — the downward diffusion of bomb-^{14}C and the upwelling of ^{14}C poor waters — it is probably more appropriate to include at least two terms to represent the cross-isopycnal transports.

4.2 Further work

As well as the possible model improvements that have been described in the previous section, there are several ways that this work could be further developed.

A global radiocarbon dataset will eventually be available from the WOCE program and this would allow the model to be extended to cover all of the oceans. If the model could be well enough constrained, it would be possible to infer the invasion rate rather than specifying it and so give a direct estimate of the air-sea flux of CO_2, although an estimate of the sea-air flux would also be required to estimate the net rate of uptake of CO_2 by the oceans.

One issue that has not been addressed here is that of how to deal with the mid-ocean crossing points. In this case, at the crossing points there were stations available on both sections at almost the same point in space and so, when estimating the geostrophic velocity, stations from different sections were not matched up. However, there are inconsistencies between the data taken from different sections, particularly in the surface and upper water column measurements which vary most strongly on a seasonal basis. For example, at the eastern end of P6 (taken during the southern hemisphere winter) the surface stations are in model layer 3 whilst at the southern end of sections P18 and P19 (taken during the autumn) the surface stations are in model layer 2. This may just be related to the seasonal shift or there could be some more systematic inconsistency between the sections.

Given the large variability that exists in this region, it seems that the compilation of time mean hydrographic data is the only way in which a good estimate of the mean circulation of this section of the ocean could be achieved. Further, separate datasets could be complied for measurements taken during El-Niño or La-Niña periods and solutions from models for the separate datasets compared to give an indication of the difference in the circulation pattern during these episodes. By separating out the

El-Niño data from other data it may be possible to place tighter constraints on the models since El-Niño is the major source of interannual variability.

Bibliography

R.S. Arthur. A review of the calculation of ocean currents at the equator. *Deep Sea Research*, 6:287–297, 1960.

Wallace S. Broecker, Tsung-Hung Peng, Gote Ostlund, and Minze Stuiver. The distribution of bomb radiocarbon in the ocean. *Journal of Geophysical Research*, 90:6953 – 6970, 1985.

Wallace S. Broecker, Stewart Sutherland, William Smethie, Tsung-Hung Peng, and Göte Östlund. Oceanic radiocarbon: Separation of the natural and bomb components. *Global Biogeochemical Cycles*, 9:263–288, 1995.

H.L. Bryden and E.C. Brady. Diagnostic model of the three-dimensional circulation in the upper equatorial Pacific ocean. *Journal of Physical Oceanography*, 15:1255–1273, 1985.

Richard A. Feely, Rik Wannikhof, and Taro Takahashi. Influence of El-Niño on the equatorial Pacific contribution to atmospheric CO_2 accumulation. *Nature*, 398:597–600, 1999.

M. Fieux, R. Molard, and A. G. Ilahude. Geostrophic transport of the Pacific-Indian oceans throughflow. *Journal of Geophysical Research*, 101:12421–12432, 1996.

E. Firing, S.E. Wijffels, and P. Hacker. Equatorial subthermocline currents across the Pacific. *Journal of Geophysical Research*, 103:21,413 – 21,413, 1998.

Alexandre Ganachaud. *Global oceanic circulation and fluxes of freshwater, heat, nutrients and oxygen.* PhD thesis, Massachusetts Institute of Technology and Woods Hole Oceanographic Institution, 1999.

D. E. Harrison. Vertical velocity in the central tropical Pacific: a circulation model perspective for JGOFS. *Deep Sea Resarch. Part 2*, 43:687–705, 1996.

Atul K. Jain, Haroon S. Kheshgi, Martin I. Hoffert, and Donald J. Wuebbles. Distribution of radiocarbon as a test of global carbon cycle models. *Global Biogeochemical Cycles*, 9:153–166, 1995.

Steven Jayne. *Dynamics of Global Ocean Heat Transport Variability.* PhD thesis, Massachusetts Institute of Technology and Woods Hole Oceanographic Institution, 1999.

Gregory C. Johnson and John M. Toole. Flow of deep and bottom waters in the Pacific at 10°N. *Deep Sea Research. Part 1*, 40:371–394, 1993.

S.A. Josey, E.C. Kent, and P.K. Taylor. A new global air-sea heat and momentum flux climatology. *International WOCE Newsletter*, 24:3–5, 1996.

Robert M. Key. WOCE Pacific Ocean radiocarbon program. *Radiocarbon*, 38:415–423, 1996.

Robert M. Key, Paul D. Quay, Gleen A. Jones, A.P. McNichol, K. F. Von Reden, and Robert J. Schneider. WOCE AMS radiocarbon I: Pacific Ocean results (P6, P16 and P17. *Radiocarbon*, 38:425–518, 1996.

Joseph Pedlosky. *Ocean Circulation Theory.* Springer-Verlag, 1996.

Tsung-Hung Peng, Robert M. Key, and H.Göte Östlund. Temporal variations of bomb radiocarbon inventory in the Pacific ocean. *Marine Chemistry*, 60:3 – 13, 1998.

S. G. H. Philander, W. J. Hurkin, and A. D. Seigel. Simulation of the seasonal cycle of the tropical Pacific ocean. *Journal of Physical Oceanography*, 17:1986–2002, 1987.

Pierre-Marie Poulain. Estimates of horizontal divergence and vertical velocity in the equatorial Pacific. *Journal of Physical Oceanography*, 23:601–607, 1993.

P. D. Quay, M. Stuvier, and W. S. Broecker. Upwelling rates for the equatorial Pacific ocean derived from the bomb ^{14}C distribution. *Journal of Marine Research*, 41:769–792, 1983.

Minze Stuiver, H. G. Östlund, Robert M. Key, and Paula J. Reimer. Large-volume WOCE radiocarbon sampling in the Pacific Ocean. *Radiocarbon*, 38:519–561, 1996.

T. Takahashi, R.A. Feely, R.F. Weiss, R.H. Wanninkhof, D.W. Chipman, S.C. Sutherland, and T.T. Takahashi. Global air-sea flux of CO_2: An estimate based on measurements of sea-air pCO_2 difference. *Proceedings of the National Academy of Sciences*, 94:8292–8299, 1997.

Peiter P. Tans, Inez Y. Fung, and Taro Takahashi. Observational constraints on the global atmospheric CO_2 budget. *Science*, 247:1431–1438, 1990.

M.N. Tsimplis, S. Bacon, and H.L.Bryden. The circulation of the subtropical South Pacific derived from hydrographic data. *Journal of Geophysical Research*, 103:21,443 – 21,468, 1998.

S.E. Wijffels. *Exchanges between hemispheres and gyres: A direct approach to the mean circulation of the equatorial Pacific.* PhD thesis, Massachusetts Institute of Technology and Woods Hole Oceanographic Institution, 1993.

S. E. Wijffels, E. Firing, and J. Toole. The mean structure and variability of the Mindanao current at 8^{o}N. *Journal of Geophysical Research*, 100:18,421 - 18,435, 1995.

Carl Wunsch. An estimate of the upwelling rate in the equatorial Atlantic based on the distribution of bomb radiocarbon and quasi-geostrophic dynamics. *Journal of Geophysical Research*, 89:7971 - 7978, 1984.

Carl Wunsch. *The Ocean Circulation Inverse Problem.* Cambridge University Press, 1996.